

Key Points:

- Some neutron suppression regions (NSRs) form from surface ice deposits while others may form through ice pumping in the sub-surface
- NSRs identified by Lunar Exploration Neutron Detector correlate well with low surface temperatures in permanently shadowed regions (PSRs) and are in agreement with sub-surface temperatures in non-PSR

Correspondence to:

P. Gläser,
philipp.glaeser@tu-berlin.de

Citation:

Gläser, P., Sanin, A., Williams, J.-P., Mitrofanov, I., & Oberst, J. (2021). Temperatures near the lunar poles and their correlation with hydrogen predicted by LEND. *Journal of Geophysical Research: Planets*, 126, e2020JE006598. <https://doi.org/10.1029/2020JE006598>

Received 3 JUL 2020
 Accepted 28 JUL 2021

© 2021. The Authors.

This is an open access article under the terms of the [Creative Commons Attribution License](#), which permits use, distribution and reproduction in any medium, provided the original work is properly cited.

Temperatures Near the Lunar Poles and Their Correlation With Hydrogen Predicted by LEND

Philipp Gläser^{1,2} , Anton Sanin³, Jean-Pierre Williams⁴ , Igor Mitrofanov³, and Jürgen Oberst^{1,5}

¹Department of Planetary Geodesy, Technische Universität Berlin, Berlin, Germany, ²Ronin Institute for Independent Scholarship, Montclair, NJ, USA, ³Institute for Space Research of Russian Academy of Sciences, Moscow, Russian Federation, ⁴Department of Earth, Planetary and Space Sciences, University of California Los Angeles, Los Angeles, CA, USA, ⁵German Aerospace Center, Institute of Planetary Research, Berlin, Germany

Abstract The lunar polar regions offer permanently shadowed regions (PSRs) representing the only regions which are cold enough for water ice to accumulate on the surface. The Lunar Exploration Neutron Detector (LEND) aboard the Lunar Reconnaissance Orbiter (LRO) has mapped the polar regions for their hydrogen abundance which possibly resides there in the form of water ice. Neutron suppression regions (NSRs) are regions of excessive hydrogen concentrations and were previously identified using LEND data. At each pole, we applied thermal modeling to three NSRs and one unclassified region to evaluate the correlation between hydrogen concentrations and temperatures. Our thermal model delivers temperature estimates for the surface and for 29 layers in the sub-surface down to 2 m depth. We compared our temperature maps at each layer to LEND neutron suppression maps to reveal the range of depths at which both maps correlate best. As anticipated, we find the three south polar NSRs which are coincident with PSRs in agreement with respective (near)-surface temperatures that support the accumulation of water ice. Water ice is suspected to be present in the upper ≈ 19 cm layer of regolith. The three north polar NSRs however lie in non-PSR areas and are counter-intuitive as such that most surfaces reach temperatures that are too high for water ice to exist. However, we find that temperatures are cold enough in the shallow sub-surface and suggest water ice to be present at depths down to ≈ 35 – 65 cm. Additionally we find ideal conditions for ice pumping into the sub-surface at the north polar NSRs. The reported depths are observable by LEND and can, at least in part, explain the existence and shape of the observed hydrogen signal. Although we can substantiate the anticipated correlation between hydrogen abundance and temperature the converse argument cannot be made.

Plain Language Summary The lunar poles have quite unique illumination conditions. For instance, the Sun never shines on some crater floors. As a consequence, the floors of those craters are very cold and dark. Here, water ice can accumulate on the surface and can be preserved for long periods of time. One of the instruments mounted on the Moon-orbiting satellite Lunar Reconnaissance Orbiter is capable of detecting areas where hydrogen is located, which is assumed to be present in the form of water ice. For instance, the instrument detected several areas at the lunar poles where a lot more water ice is found than at other locations. For these special locations, we calculated the temperatures at the surface and near sub-surface to see whether they are indeed cold enough for water to freeze. At some of these locations, surface temperatures turn out to be too warm. However, we found that at these warm surfaces where no water ice can exist it can be transported into the sub-surface and survive there. This mechanism is referred to as ice pumping. In summary, we could show that temperatures at all these special locations are usually cold enough for water ice, either right at the surface or within the first meter of soil.

1. Introduction

1.1. Lunar Polar Environment

The lunar poles offer a unique environment where extreme illumination and thermal conditions exist in immediate vicinity to each other. Owing to the small lunar axial tilt of 1.5° with respect to the ecliptic, permanently shadowed regions (PSRs) exist in many polar craters (Bussey et al., 2010; Mazarico et al., 2011; Noda et al., 2008). Consequently the coldest temperatures at the Moon are found within these craters (Paige

et al., 2010) where the lowest temperatures reach 20 K (Siegler et al., 2015; Williams et al., 2019). On crater rims of such PSRs, however, persistently illuminated areas can exist offering sunshine at surface level for 80%–90% of the year and even >90% at 2 m above ground (Gläser et al., 2014, 2018). Here, temperatures of ≈ 30 K (Gläser & Gläser, 2019) are possible and hence these areas differ significantly in illumination and thermal conditions to the nearby PSRs. The orientation of the lunar orbital and spin axis has undergone significant changes over its history which directly defines the thermal environment of the Moon, especially at the poles (Siegler et al., 2011).

1.2. Volatile Sources, Migration, and Cold Trapping

Over half a century ago Watson et al. (1961) postulated the theory that water ice can be cold-trapped in lunar polar craters. Arnold (1979) proposed four potential sources for said lunar H₂O which are still valid today: solar wind reduction of iron (FeO), H₂O delivery by asteroids and/or comets, and degassing of endogenic water from the lunar interior. Independent of the source, in each of the four scenarios water molecules need to migrate to the cold polar areas in order to become trapped within PSRs. Butler et al. (1993) and Butler (1997) showed that 20%–50% of water molecules survive the migration to the poles via ballistic hops and accumulate in cold traps. Needham and Kring (2017) estimated that volcanically derived volatiles alone, degassed during mare basalt forming eruptions, could account for all currently observed hydrogen deposits in lunar PSRs. However a more recent study by Head et al. (2020) suggests volatile-rich impactors to be the main source of polar volatiles rather than volcanically derived volatiles. Crider and Vondrak (2002) showed that water deposits implanted by the solar wind proton flux within 100 Ma could also account for all hydrogen detected by the Lunar Prospector Neutron Spectrometer (LPNS; Feldman et al., 1998). Ong et al. (2010) calculated the delivery of water via asteroidal and cometary impacts and found that either delivery mechanism could account for the observed hydrogen content by LPNS.

Those 20%–50% water molecules which survive the migration toward the poles (Butler, 1997; Butler et al., 1993) and accumulate in cold traps (Watson et al., 1961), are still prone to be redistributed or be lost to space via disruption by sputtering, impact gardening, sublimation, and bombardment by UV radiation (Ong et al., 2010). At temperatures of 106.6 K, for instance, it would take one billion years for a ≈ 1 mm thick ice layer to evaporate (Zhang & Paige, 2009, 2010). Killen et al. (1997) however showed that for temperatures <112 K the delivery of water from meteoroids and asteroids equals or even exceeds the loss rate. Such low temperatures are commonly found within PSRs (Paige et al., 2010) suggesting that water ice cannot only be trapped there but also survive geologic time-scales. Zhang and Paige (2009) point out that the temperature range over which simple organics can be cold-trapped is much wider than that of water ice and also covers the volatility temperature of water ice. They conclude that simple organics could therefore be present in areas which are currently too warm for water ice.

1.3. Observations

It took more than 30 yr after water ice was first thought to exist on the Moon until a series of remote sensing techniques was applied to detect and quantify potential deposits (e.g., Benna et al., 2019; Clark, 2009; Farrell et al., 2019; Feldman et al., 1998; Fisher et al., 2017; Hayne et al., 2015; Mitrofanov et al., 2010; Nozette et al., 1996; Paige et al., 2010; Pieters et al., 2009; Thomson et al., 2011; Zuber et al., 2012). Although findings of the aforementioned authors and missions are plentiful, they cannot unambiguously be assigned to the presence of water ice but different explanations can be given, for example, roughness, fresh surface material, hydroxyl (OH) bearing minerals, etc. So far, direct evidence for surface exposed water ice comes from two remote sensing instruments, the Moon Mineralogy Mapper (M³) flown on the Chandrayaan-1 spacecraft (Li et al., 2018) and the NASA/DLR Stratospheric Observatory for Infrared Astronomy (Honniball et al., 2020). Additionally and most crucially, there is unambiguous evidence for significant amounts of lunar near-surface water ice in Cabeus crater measured in-situ by the Lunar Crater Observation and Sensing Satellite (LCROSS; Colaprete et al., 2010). Cabeus' crater floor is a PSR and was selected as the LCROSS impact site due to elevated levels of hydrogen reported by both, the LPNS (Eke et al., 2009; Feldman et al., 1998) and the Lunar Exploration Neutron Detector (LEND; Mitrofanov et al., 2010).

PSRs are all found near the poles in which temperatures generally are such that water ice can exist at surface level. However, Mitrofanov et al. (2012) showed that hydrogen-rich regions, the so-called neutron suppressed regions (NSRs), as identified by LEND do not necessarily coincide with PSRs. Surprisingly they can also be found in non-PSR areas where temperatures are too high for water ice to exist. Although these occasionally sunlit NSRs are found near both lunar poles, the most prominent ones are located at the north pole, where additionally most PSRs do not show enhanced neutron suppression. However, there are several studies (Eke et al., 2012; Lawrence et al., 2011; Teodoro et al., 2014) skeptical of the correct reduction and interpretation of LEND observations as proposed by Mitrofanov et al. (2010), specifically of the observations made by the collimating detectors which are primarily used to create polar maps at high spatial resolution. In a direct response to the raised concerns by Lawrence et al. (2011) and Mitrofanov et al. (2011) presented additional evidence supporting their earlier results. Later studies (Litvak et al., 2012, 2016; Livengood et al., 2018) could show further that LEND indeed measures a significant amount of collimated epithermal neutrons and represents an appropriate data set to be used for mapping hydrogen at higher spatial resolution than was possible with LPNS (Litvak et al., 2012). Therefore, we decided to use the previously published LEND data (Sanin et al., 2017) to carry out the presented analysis.

Supporting evidence for the lack of hydrogen deposits in north polar PSRs is given in a study by Rubanenko et al. (2019). They evaluated depth-to-diameter ratios of simple craters at Mercury and the Moon and found that they become distinctively shallower from 75°N/S on polewards. The shallowing is due to infill within the craters which is most convincingly explained by water-ice deposits. Only for the lunar north pole such shallowing could not be confirmed suggesting (almost) ice-free craters. A study by Schorghofer and Aharonson (2014) shows a mechanism how water-ice can be diffused into the sub-surface in sunlit areas if the maximum and average temperatures stay above 120 K and below 105 K, respectively. Regions offering such conditions can only be found near the lunar poles and cover an area larger than the one occupied by PSRs.

We investigate LEND data in combination with temperature maps. Here, we compile surface and sub-surface temperature maps since the depth to which neutron remote sensing can detect hydrogen is down to ≈ 1 m of planetary regolith (Litvak et al., 2016). We aim to answer the open question whether or not the identified hydrogen-rich areas in sunlit areas are due to neutron signals stemming from deeper layers where temperatures might be cold enough for water ice to exist.

2. Data and Method

For our study, we created high-resolution lunar polar LOLA DTMs (Gläser et al., 2013) centered on the poles. Both DTMs span 650×650 km and have an original resolution of 20 m/pixel. The resolution was downsampled to 200 m/pixel to accommodate limitations in computational capabilities. We defined a total of eight regions of interest (RoIs) for which we report illumination and temperature. The RoIs comprise the central 50×50 km subsets of each DTM (see Figures 1e and 2e) as well as regions inside of Cabeus, Haworth, and Shoemaker craters at the south pole and nearby Peary, Fibiger, and Whipple craters at the north pole. The central regions were chosen due to the extreme illumination conditions found right near the poles which also translate into extreme temperatures, hot and cold. The remaining RoIs were chosen based on studies using data from LEND which identified them as NSRs (Mitrofanov et al., 2012; Sanin et al., 2017). In fact, Sanin et al. (2017) reported a total of seven NSRs for the north pole and eight for the south pole which we all analyzed but only report on a few of them. A map of the NSRs which are not further discussed in this study is shown in Figure A1. For the south pole we chose to report on the three NSRs with deepest suppression which, in descending order, are Cabeus, Shoemaker, and Haworth. For the north pole, we chose to report on the two most suppressed regions which are located near Peary (referred to as Erlanger by Sanin et al., 2017) and Fibiger crater. The third NSR we chose is located near Whipple crater and is the fourth most suppressed region in the north, together with an unnamed region. We did not choose the third most suppressed region, referred to as Plaskett, since it is located right on the boundary of the LEND and temperature data available for this study.

The chosen south polar NSRs correlate (lie within and spread outside) with large, permanently shadowed craters. In our study, we refer to such sites as “classical” NSRs since they reside in PSRs of large and cold crater floors which are generally assumed to be the most promising places to contain water ice (e.g.,

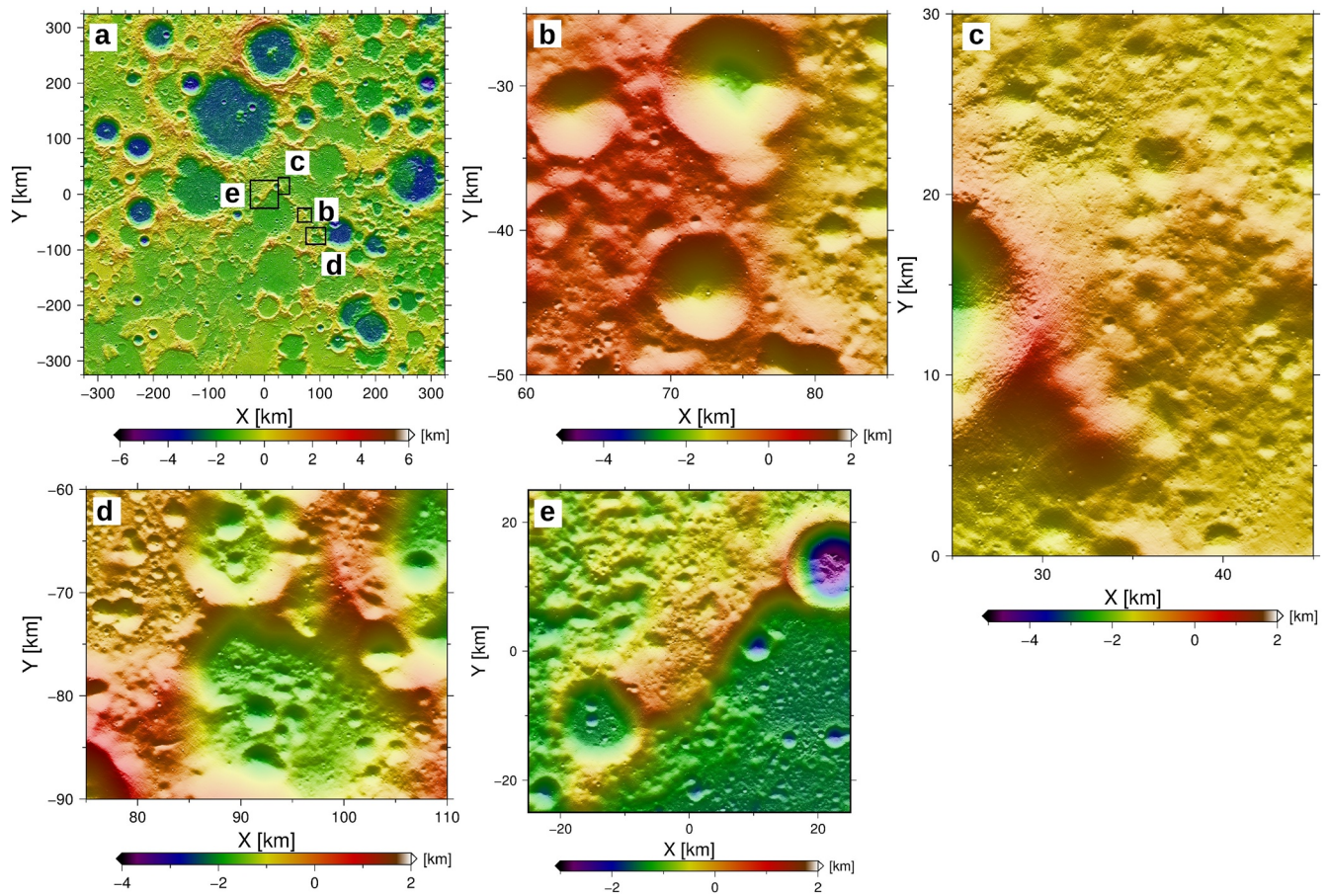


Figure 1. The north polar LOLA DTMs have a resolution of 20 m/pixel. (a) 650 × 650 km north polar DTMap with outlines of RoIs. The RoIs are (b) Peary, (c) Whipple, (d) Fibiger craters, and (e) the central polar 50 × 50 km region. All maps are displayed in gnomonic map projection and are color-coded by heights. For presentation purposes the map sizes are arbitrary and are not related to each other.

Arnold, 1979; Watson et al., 1961). However, we find four of the eight south polar NSRs to be atypical and one NSR resides outside our DTMap and was excluded (see Figure A1). We define NSRs to be atypical if they reside in areas which occasionally receive direct sunlight and experience surface temperatures that are too warm for water ice to exist. Our chosen north polar NSRs do in fact reside in warmer non-PSR areas (Boyn-ton et al., 2012; Sanin et al., 2012). In total there are four atypical and two classical NSRs at the north pole and 1 NSR resides outside our DTMap and was excluded from the study (see Figure A1).

The RoIs are synthetically illuminated (Gläser et al., 2014, 2018) at 12-h increments over a 19 yr time frame to cover all seasonal and orbital illumination conditions (note: the lunar precessional cycle lasts 18.6 yr). Illumination is derived for each RoI considering obstructions of the Sun by topography from the respective entire polar 650 × 650 km DTMap. Note that we treat the Sun as an extended source taking into account the solar-limb darkening effect. At each pixel and time step the instantaneous illumination is used as an input to subsequently solve a one-dimensional representation of the heat equation to model temperatures. In our model (see Gläser & Gläser, 2019 for more details) we consider heat conduction in the upper 2 m of regolith and derive temperatures for a total of 30 layers, 29 layers in the sub-surface and 1 layer at the surface (compare the first 27 layers given in the first column of Table B2 plus the additional layers at 1.25, 1.55, and 1.85 m, respectively). Thermophysical parameters were adopted from studies of Vasavada et al. (2012) and Hemingway et al. (1973). Multiple scattering of reflected sunlight by terrain as well as thermal re-radiation is considered within a window size of 50 × 50 km. Scattering of sunlight from Earth and thermal re-radiation of an average warm Earth are also considered (Gläser & Gläser, 2019; Trenberth & Stepaniak, 2003). Finally, heat stemming from nuclear decay in the lunar interior is modeled via a constant radiogenic heat source of 0.016 W/m² sitting just below our deepest layer (Langseth et al., 1976; Vasavada et al., 2012). The

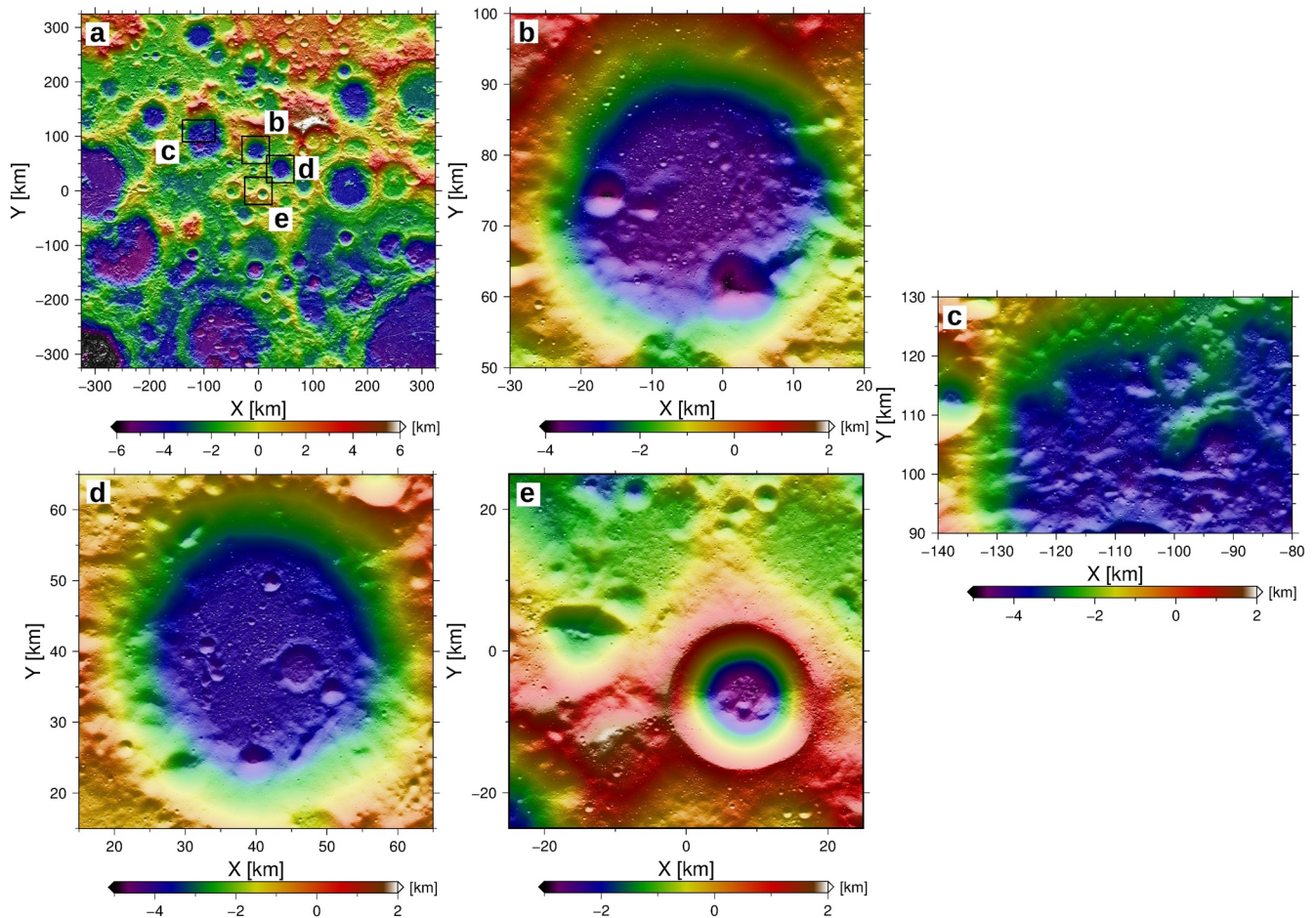


Figure 2. The south polar LOLA DTMs have a resolution of 20 m/pixel. (a) 650 × 650 km south polar DTM with outlines of RoIs. The RoIs are (b) Haworth, (c) Cabeus, (d) Shoemaker craters, and (e) the central polar 50 × 50 km region. All maps are displayed in gnomic map projection and are color-coded by heights. For presentation purposes the map sizes are arbitrary and are not related to each other.

model and the chosen parameters are capable of reproducing the Diviner temperature measurements (see Gläser & Gläser, 2019).

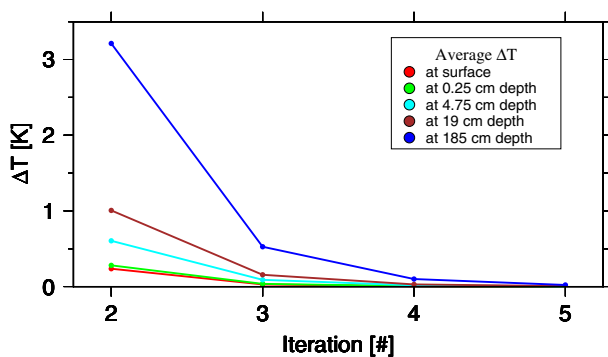


Figure 3. The average temperature difference at five different depth layers (0, 0.25, 4.75, 19, and 185 cm, respectively) is shown over five iterations. All profiles converge toward zero with the deepest layer starting from the largest difference. Profiles correspond to the central regions of interest (RoI) at the north pole but are representative for all RoIs presented here.

3. Results

We started our investigation from a uniform temperature distribution at each of the 30 layers. The surface layer was set to 80 K with temperature declining by 1 K per layer. Hence the deepest layer (30 cm wide and centered at 1.85 m in the sub-surface) started from a uniform temperature distribution of 51 K. The DTMs were then illuminated in 12-h time-steps for 19 yr in order to cover all effects stemming from the 18.6 yr lunar precessional cycle. The chosen time period was January 01, 1991 at midnight to January 1, 2010 at midnight for which roughly the same orbital, seasonal, and hence the same illumination conditions occur at the start and end date. Consequently, we can start to iterate with the last result as our new initial temperature distribution. We found that after five iterations (i.e., 95 a) the largest temperature difference from the fourth to the fifth iteration was 0.5 K at the deepest layer and 0.02 K at the surface with average values being one to two orders of magnitude smaller, see Figure 3. Hence, the solution after the fifth iteration is considered our equilibrated

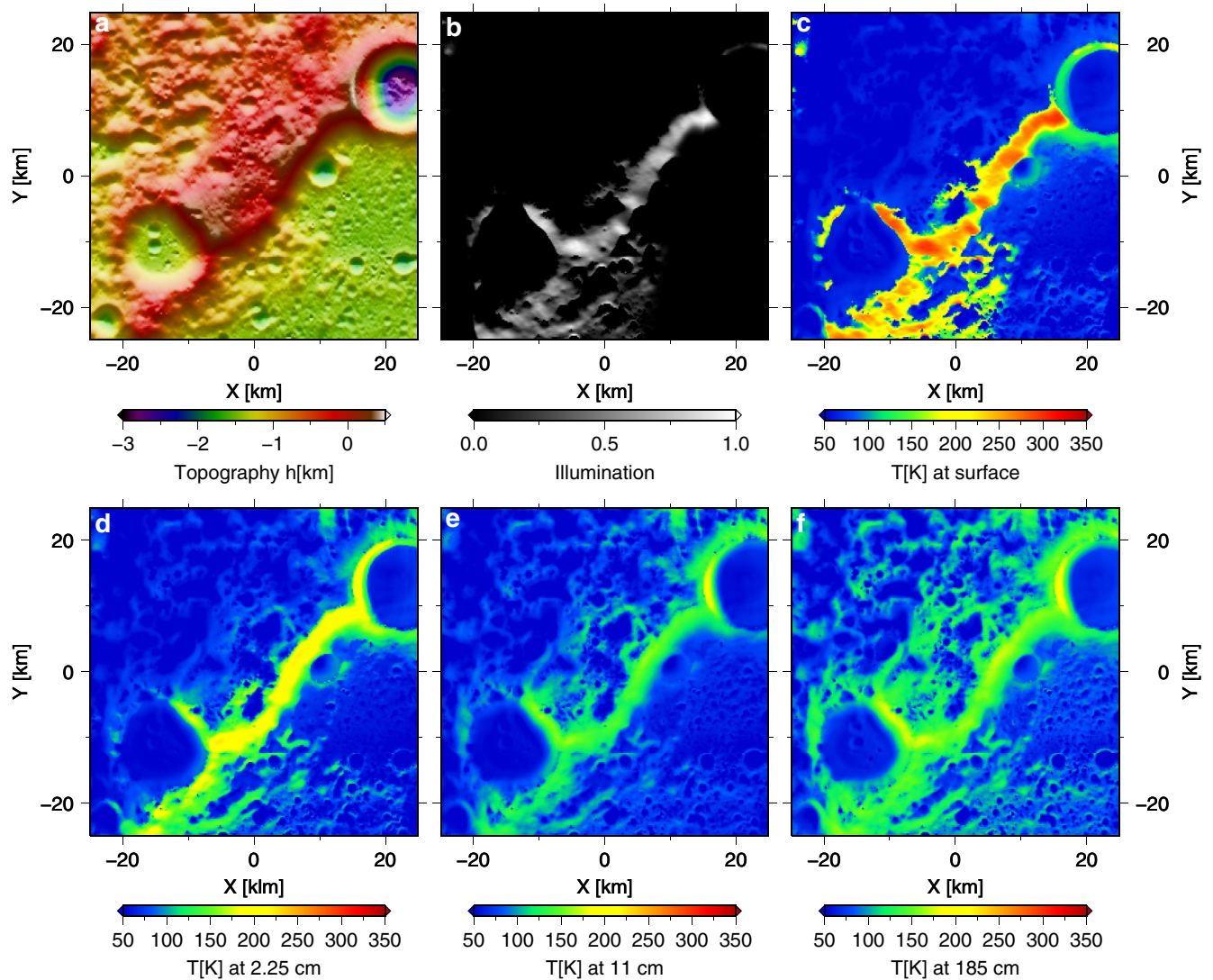


Figure 4. The equilibrated solution (fifth iteration) for the north polar regions of interest (RoI) at January 1, 2010 at midnight. (a) The topography of the RoI for context (same as in Figure 1e). (b) Illumination. Temperature at (c) Surface, (d) At 2.25 cm depth, (e) At 11 cm depth, (f) At 185 cm depth. Maps are centered at the north pole in gnomonic map projection and are color-coded by (a) heights, (c)–(f) temperature, and (b) gray-scaled and normalized by maximum insolation (444.49 W/m^2).

solution from which we derived all results presented in this study. In Figure 4, the instantaneous illumination and temperature at midnight on January 1, 2010 for the central north polar RoI is displayed at four different depths. While the hottest surface temperatures correspond directly to sunlit areas (Figure 4c), the sub-surface layers show quite a different temperature distribution. Here, a convolution of many previously conducted temperature patterns is preserved through the low conductivity of the cold upper surface layers and the feasibility of the sub-surface regolith to store heat for longer time-scales, that is, no direct radiation into space.

3.1. Temperature Maps

Starting from the equilibrated solutions at each RoI, we derived instantaneous, average, depth-to-ice (see Section 3.2), minimum and maximum temperature maps over the same 19 yr period (see Figures 5 and 7). In Figure 5, we show the maximum temperatures reached within our considered time-frame at four different depths (surface, 2.25 cm, 11 cm, and 1.85 m) for the central RoI at the south pole. At surface level the maximum temperatures range here from 23.35 to 339.07 K and attenuate from 27.91 to 191.77 K at 185 cm

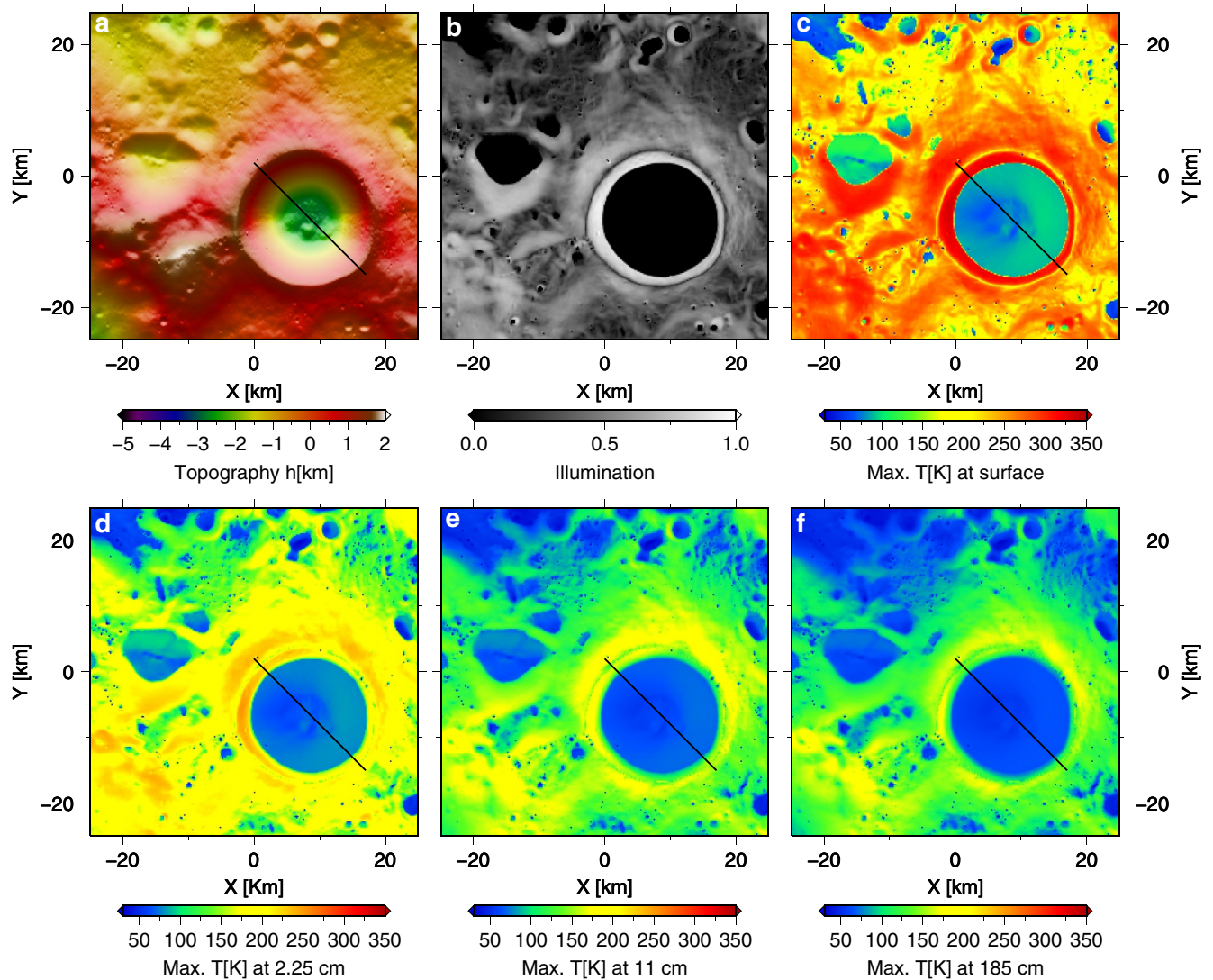


Figure 5. Maximum temperatures reached over the considered time-frame at the central south polar regions of interest (RoI). (a) The topography of the RoI for context. (b) Maximum illumination. Maximum temperature at (c) Surface, (d) At 2.25 cm depth, (e) At 11 cm depth, and (f) At 185 cm depth. Maps are centered at the south pole in gnomonic map projection and are color-coded by (a) heights, (c–f) temperature, and (b) gray-scaled and normalized by maximum insolation (719.53 W/m^2). The black line is the location of the temperature profiles displayed in Figure 7.

depth, respectively (see Figures 5c and 5f). Table B1 lists the extremes of the minimum, average and maximum temperature maps at four selected depths for all eight considered RoIs.

Note that minimum temperatures at each RoI are identical at each depth layer (compare minimum temperatures at each RoI in Table B1). These static temperature profiles are found in permanently, doubly shadowed regions where the only remaining heat flux is stemming from internal heat sources preventing them from cooling down even further. At these locations no additional fluxes from multiple scattering or Earth shine occur making them the darkest and coldest spots on the Moon (Siegler et al., 2015). The theoretical minimum temperature of 23.05 K at surface level, neglecting conduction and considering only an internal heat flux of 0.016 W/m^2 , is defined by the Stefan-Boltzmann-Law. Since we have not yet reached the theoretical minimum temperatures with our model (compare minimum temperature in the “surface” column of Table B1) additional simulation iterations might be necessary to achieve absolute equilibrium. However, the differences are considered marginal, for example, the maximum theoretical difference is 0.3 K , and as stated before we assume to have an equilibrated solution.

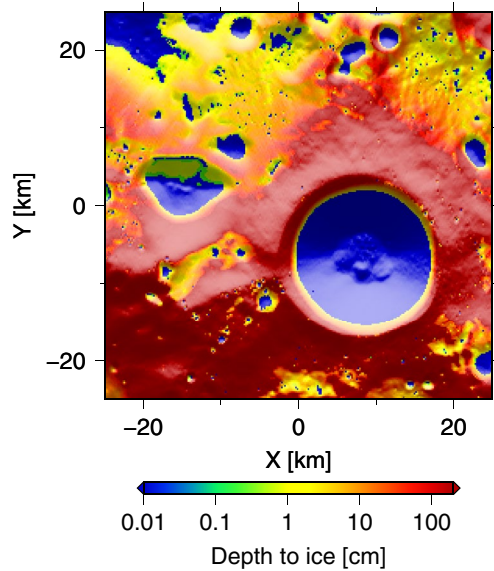


Figure 6. Depth-to-ice (depth at which $T < 110$ K) in centimeters for the central south polar regions of interest derived from 30 stacked maximum temperature maps from surface level down to 185 cm depth. In permanently shadowed regions potential ice can generally be found at surface level, for example, Shackleton crater. At 2/3 of the shown area water ice could be stable at depth shallower than 1 m.

As expected the highest temperatures occur in sunlit areas on the surface (compare maximum temperatures at “surface” column with the other columns in Table B1). Here, temperatures attenuate drastically with depth (read maximum temperatures of each line given in Table B1 from left to right). Average temperatures are relatively constant in all layers and are virtually identical to the maximum temperature at the lowest surface layer at 1.85 m depth (compare average and maximum temperatures given in last column of Table B1). Here, temperature changes do not occur anymore and temperatures remain constant with respect to diurnal, seasonal, and precessional cycles.

3.2. Depth-to-Ice Maps

Based on maximum temperature maps of each of our 30 layers (e.g., Figure 5) depth-to-ice maps can be inferred. For this purpose we stacked all maximum temperature maps and searched from the top to the bottom layer at which depth the temperature dropped below 110 K (Paige et al., 2013). We chose this temperature as the limit for the stability of water ice deposits (Killen et al., 1997; Vasavada et al., 1999). From Figures 5b and 6, we can infer that large areas of the central south polar RoI, for example, the inside of Shackleton crater, do not receive any direct illumination and classify as PSRs. Here, typical depths at which water ice could be stable are either at surface level or within the upper 1 cm (see Figure 6). Temperatures at roughly 70% of the shown area are such that water ice would be stable at depth shallower than 1 m. In fact, depth-to-ice maps of the north pole of Mercury have shown that most of its water

ice deposits south of 83°N would be thermally stable only if buried beneath a ≈ 10 cm thick layer, which is consistent with findings from radar observations (Harmon, 2007; Paige et al., 2013). The model parameters and temperature threshold which Paige et al. (2013) adopted in their study are similar to the ones used in our study.

Temperature profiles through Shackleton crater, indicated in Figures 5a and 5c–5f as a black line, are shown in Figure 7. These lateral profiles are taken along each individual depth layer and are not to be confused with the vertical profiles derived from stacking all depth layers, as shown in Figure 3. For the lateral profiles we report the maximum, average and minimum temperatures at our four chosen depth layers. For instance, Figure 7a shows temperature profiles at the surface where the maximum temperature profile (red) reaches temperatures > 300 K outside the PSR and drops to < 100 K inside the PSR. The average (green) and minimum (blue) temperature profiles follow the same trend as the maximum temperature profile but at much lower temperatures with smaller amplitude variations. The topographic profiles (black) are highlighted (cyan) where the maximum temperature is below 110 K indicative for locations where stable water ice could be found. We find maximum surface temperatures that allow water ice to be stable at most locations along the profile (see Figure 7a). The temperature profiles slowly converge with increasing depth and at 185 cm depth they are virtually identical, that is, temperature does not change anymore with the diurnal, seasonal, and precessional cycle (see Figure 7d and Table B1).

At the crater rim temperature drops lower than on the steep crater walls since the solar incidence angle is basically perpendicular which leaves small craters in permanent shadow acting as so-called micro cold traps. Micro cold traps are commonly referred to as PSRs in craters on scales of < 100 m which make up the significant part of 10% of the area of all lunar PSRs (Hayne et al., 2020). Additionally, it is here on Shackleton’s rim where we generally also find locations with extended and continuous periods of illumination offering the possibility to charge batteries of rovers and landers relying on solar panels (Gläser et al., 2014, 2018). Shackleton’s extensively illuminated crater rim in combination with nearby located micro cold traps could serve as a prime future landing site (Gläser et al., 2018). Here, rovers with drilling capabilities could reach such potentially water-ice-bearing sites on the rim without traversing down the steep walls of Shackleton crater. Although temperatures would allow for water ice to be stable at a vast area inside the PSR of Shackleton

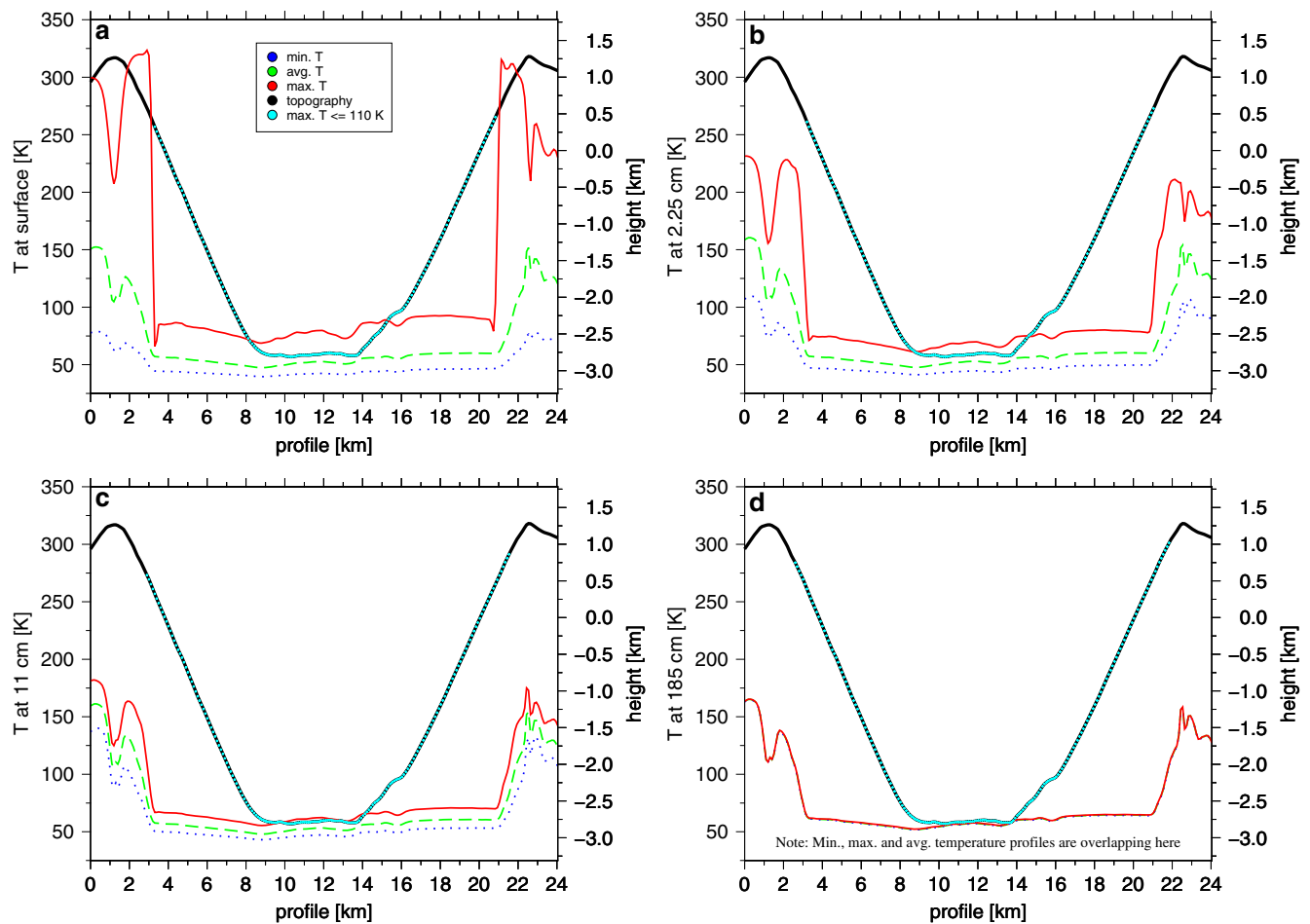


Figure 7. Profile through Shackleton crater as indicated by the black lines in Figure 5. Each plot shows (solid black) the topographic profile, (solid red) maximum temperature profile, (dashed green) average temperature profile, (dotted blue) minimum temperature profile, and (dashed cyan) the location on the topographic profile at which water ice can be stable. Profiles correspond to (a) Surface, (b) 2.25 cm depth, (c) 11 cm depth, and (d) 185 cm depth.

and also at shallow depth on its crater rim, there is no scientific consensus whether or not water ice is at all present (e.g., Fisher et al., 2017; Haruyama et al., 2008, 2013; Hayne et al., 2015; Li et al., 2018; Miller et al., 2014; Spudis et al., 2013; Thomson et al., 2012; Zuber et al., 2012).

3.3. Hydrogen Maps

Temperature alone is not definitive evidence for the presence of lunar water ice (Eke et al., 2014; Lawrence, 2017). Therefore, in this study, we incorporate LEND observations to provide an additional constraint. LEND measures the neutron leakage of the Moon allowing the detection of hydrogen present within the upper ≈ 1 m of regolith (Litvak et al., 2016). Sanin et al. (2017) introduced the suppression parameter ξ which represents the ratio between the average neutron counting within LEND's field-of-view to the average neutron counting of a hydrogen-poor reference area. This parameter anti-correlates with the hydrogen concentration in the soil—it is close to one for hydrogen-poor areas and decreases in areas with hydrogen-rich soil. Maps of the suppression parameter ξ have an original resolution of 0.501° in longitude (≈ 7.75 km at 89°) and 0.0625° in latitude (≈ 15 km) and are shown in Figure 8. Note the three selected NSRs at each pole that have distinctively lower counts than their surroundings. Here, the lower counts stem from a relatively larger hydrogen abundance, presumably water ice, efficiently moderating the neutron flux (e.g., Mitrofanov et al., 2010, 2012). The central north polar RoI shows faint neutron suppression along the equator-facing rim of Peary crater. Although suppression parameters in the vicinity of NSRs and in the polar areas in general are $\xi \approx 0.9$ (see Figure 8) they are considered too faint to be classified as an NSR. Contrary,

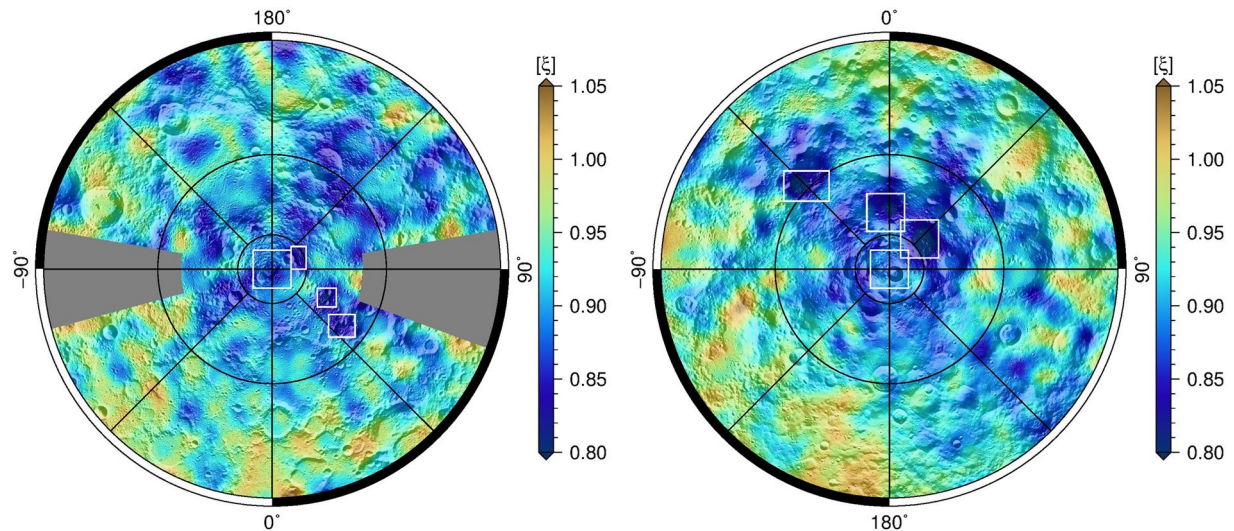


Figure 8. Maps of suppression parameter ξ derived from neutron counts measured by Lunar Exploration Neutron Detector. Regions of interest (RoIs) are shown within white boxes. (Left) North polar map of ξ with the central RoI and three neutron suppressed regions (NSRs) denoted as Fibiger, Whipple, and Peary. The gray areas are left out due to poor statistics of neutron measurements in these regions (see Sanin et al., 2017). (Right) South polar map of ξ with the central RoI and three NSRs denoted as Cabeus, Haworth, and Shoemaker.

inside NSRs we find suppression parameters of $\xi \approx 0.8$. The central south polar RoI including Shackleton crater does show some suppression, however, there is no such distinct neutron suppression as for the three south polar NSRs although temperatures would allow for stable surficial water ice (see Figures 5 and 6). Although LEND data shows faint neutron suppression at Shackleton crater it is in contrast to the findings of Miller et al. (2014). In their study, based on LPNS data, they report bulk surface hydrogen enhancements for Shackleton crater and contrary find no evidence for enhanced neutron suppression at Haworth and Shoemaker crater (two of our chosen NSRs). Litvak et al. (2012) notes that LEND and LPNS correlate well on the global scale but can differ on local scale. Note also that LEND's reported resolution (≈ 10 km), however disputed by Lawrence et al. (2011), is much finer than that of LPNS (≈ 46 km; Litvak et al., 2012).

3.4. Synthesis

If LEND data shows ancient water ice content of the lunar upper ≈ 1 m of regolith and water ice is stable for geological time-scales at temperatures below 110 K then correlation is expected between (sub)-surface temperature and LEND's neutron count maps and derivatives of it, for example, neutron suppression maps. Consequently we compared our temperature maps at each of the 30 layers to LEND neutron suppression maps to reveal the range of depths at which both maps correlate best (see Figure 10).

Based on the fact that the LCROSS impact site (longitude -48.7093° , latitude -84.6796° Marshall et al., 2011) at which water ice concentrations of $\approx 5.6 \pm 2.9\%$ by mass (Colaprete et al., 2010) were found lies in a region of suppression parameters $\xi = 0.77$, we define this value as a clear sign of water ice (see impact location in Figure A6). Consequently, we could use the value of $\xi = 0.77$ found at the impact site of LCROSS and be confident that we find similar amounts of water ice whenever we encounter such suppression parameters. However, $\xi = 0.77$ is the deepest suppression parameter found anywhere on the Moon and is only present at the impact site within Cabeus crater. From LEND observations we know that the deepest suppression parameters at the identified NSRs (Sanin et al., 2017) range from $\xi = 0.77 \pm 0.02$ at Cabeus to $\xi = 0.84 \pm 0.03$ at Idel'son L. In order to derive a conservative threshold for the suppression parameter at which we still expect to find substantial amounts of water ice beyond Cabeus crater, we chose the upper limit of the average of the reported deepest suppression parameters derived from those NSRs that are also completely covered by our DTM. We find the average to be $\xi = 0.815 \pm 0.019$ and hence set our threshold to the rounded upper limit $\xi = 0.83$. To further support the use of the threshold value of $\xi = 0.83$ we derived histograms of depth-to-ice calculations from Diviner temperature data (Paige et al., 2010, 2018) for regions within 10° of the poles and for the regions coinciding with neutron suppression parameters of $\xi \leq 0.83$ (see Figure 9).

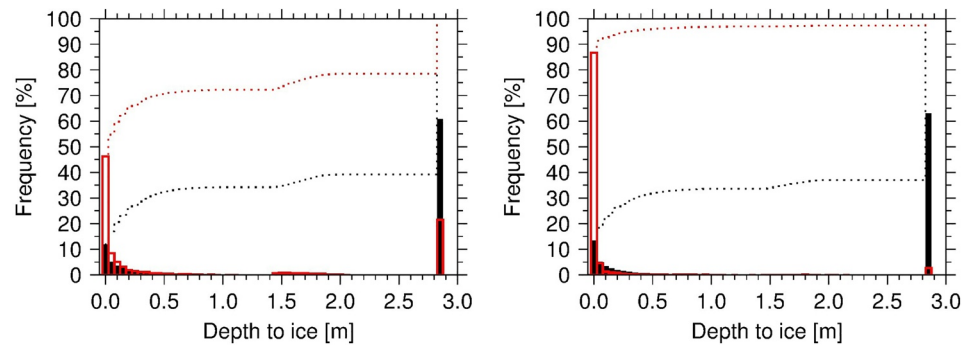


Figure 9. (Cumulative) histograms of depth-to-ice calculations derived from Diviner temperature observations and modeling. The histograms for the region within 10° of the pole are shown in black. In the Diviner depth to ice maps, depths deeper than 2.8738 m are not calculated and are aggregated in that bin. The histogram for regions defined by neutron suppression parameters below our chosen threshold value of $\xi = 0.83$ are shown in red. Left: The histograms of the north polar region. Right: The histogram of the south polar region.

The histograms of the regions which we define as containing water ice are clearly shifted toward ice stability depths closer to the surface (<0.5 m) and hence coincide with colder (near)-surface temperature than the background polar region. The histogram of regions defined by $\xi = 0.83$ also reveals that most reported depths at which ice can be stable are found within the upper 1 m of the regolith, the depth to which LEND can detect hydrogen. Further we note that we performed a two-sample Kolmogorov-Smirnov test which revealed that the histograms of depth-to-ice measurements of the polar background and the NSRs come from different populations ($\alpha = 0.01$). The investigated NSRs are therefore also unique with regards to their temperature distribution in the (sub)-surface. We conclude that the chosen value is an appropriate threshold in the search for water ice.

The model by Sanin et al. (2017) suggests that a suppression parameter of $\xi = 0.83$ corresponds to 0.37% by mass of water uniformly distributed in the sub-surface soil. They also show that by increasing the thickness of the dry top layer and placing the ice uniformly below it, the water ice concentrations of $\approx 5.6 \pm 2.9\%$ by mass measured by LCROSS can be reproduced.

For our analysis we derived maximum temperatures over the 19 yr period and mapped possible water ice locations based on temperature (where $T \leq 110$ K) and on neutron suppression parameters (where $\xi \leq 0.83$) at four different depths for our eight polar RoIs (see Figures A2–A9). We chose to display depth layers at surface level, 2.25, 11, and 95 cm depth up to which LEND is able to detect the presence of hydrogen. The central polar RoIs which are not classified as NSRs are shown in Figures A2 and A3. The three chosen south polar NSRs can be labeled as “classical” NSRs; they reside within the PSRs of large, cold crater floors see (Figures A4–A6). Our three north polar NSRs, however, can be labeled as atypical since they are all found in non-PSR areas (see Figures A7–A9).

Stable water ice reservoirs are mainly defined by temperature (Hayne et al., 2015) which in our case, where we have estimates for sub-surface temperatures, provides information about the depth at which potential water ice is expected to be found, that is, $T \leq 110$ K. On the other hand a neutron suppression parameter of $\xi \leq 0.83$ indicates the actual presence of hydrogen, here assumed to be present in the form of water ice. As neutron observations provide no information at which depth or range of depths the suppression parameter is prevalent, that is, where the water ice reservoir is located, we want to constrain those boundaries by co-evaluating suppression parameters and temperatures (see Figure 10).

However, since LEND can observe neutrons to depths of 1 m, the observed water ice content must already be present within that depth even if the reservoir continues to even greater depths. Further, there is evidence that water ice is distributed heterogeneously in the regolith such that it is expected to find a range of depths at which ice is present (Hurley et al., 2012). With the aim of finding the bulk range of depths responsible for the LEND signal, we derived growth rates for the fraction of the overlap between potential water ice areas, defined either by $T \leq 110$ K or by $\xi \leq 0.83$ (Figure 11). We chose growth rate as a tool to derive a depth level up to which we assume contributions to the observed LEND signal. Here, we defined

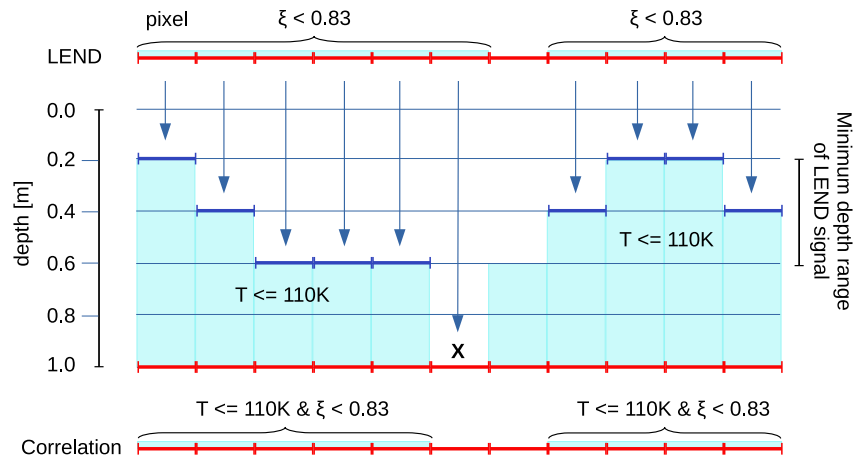


Figure 10. The concept of how to derive the minimum range of depths from which the Lunar Exploration Neutron Detector (LEND) signal originates. At the top, we find LEND to observe hydrogen content with neutron suppression parameters of $\xi \leq 0.83$ (cyan) in 10 of 11 pixels (red). The middle part shows the distribution of regions within the upper 1 m of regolith along five depth layers that have temperatures of $T \leq 110\text{ K}$ (cyan squares). At the bottom we show at which pixels LEND signals of $\xi \leq 0.83$ and layers with temperatures of $T \leq 110\text{ K}$ correlate, that is, 9 from 10 pixels (90%) at which LEND observed hydrogen. On the right hand side we find the minimum range and the minimum depth which can describe the LEND signal and hence where we report water ice to be located, for example, a range of 40 cm and a minimum depth of 60 cm. Note: That in our example the central pixel at which LEND measures hydrogen content does not correlate with low temperature.

that if the overlapping fraction grows $< 0.1\%/cm$ with increasing depth then we consider to have found the minimum deposit depth of the suppression region at which we consider no further contribution to the LEND signal. We found that threshold by visually examining Figure 11 where profiles are asymptotic to the x -axis. Note that we report a minimum deposit depth at which we assume the entire LEND signal to be explained by water ice heterogeneously distributed from surface to said depth, however, water ice might as well be present below that depth.

For the south polar NSRs it is noticeable that large parts of the areas confined by the contour lines of $T = 110\text{K}$ and $\xi = 0.83$ are coincident at surface level already (see Figures A4–A6 and also Table B2). Especially at Haworth crater the strong hydrogen signal is completely within the contour lines of $T = 110\text{ K}$, which we interpret as possible evidence for (near)-surficial water ice. Here, deeper layers might not add a significant contribution to the observed LEND signal. At Shoemaker crater, areas confined by the contour lines of $T = 110\text{K}$ and $\xi = 0.83$ at surface level overlap 72.4% (see Table B2) but there is still a strong hydrogen signal where surface temperatures are too hot. At 11 cm depth the area within the $T = 110\text{ K}$ contour line matches well with the area confined by the $\xi = 0.83$ contour line. Consequently, the top $\approx 10\text{--}20\text{ cm}$ of

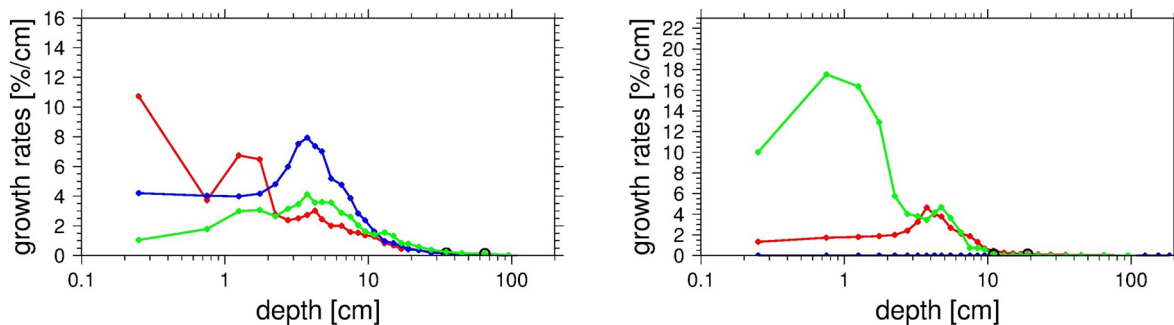


Figure 11. Growth rates in $\%/cm$ of the overlapped fraction of neutron suppressed regions (NSRs) by layers of cold temperatures ($T < 110\text{ K}$). Left: north polar craters Peary (red), Fibiger (blue), and Whipple (green). Right: south polar craters Shoemaker (red), Haworth (blue), and Cabeus (green). The atypical NSRs at the north pole continue to grow their overlapped area with cold layers in depths below 10 cm. For the classical NSRs at the south pole growth rates decrease quickly below depths of $\approx 4\text{ cm}$. Note the excessive growth rates of Cabeus in the first 2 cm where the absolute overlap grows by $\approx 30\%$.

regolith, including the surface itself, provide a thermal environment which could explain LEND's observed hydrogen signal. In fact, we find that below 19 cm depth the overlapping area of the neutron suppression region (NSR) $\xi \leq 0.83$ and cold temperatures $T \leq 110\text{K}$ has reached 95.56% (see Table B2). Here, at greater depths the overlap does not significantly grow any further, that is, the growth rate drops below our chosen limit of 0.1%/cm (see Figure 11b). Nevertheless we want to point out that the growth rate only identifies the minimum depth at which the lateral extent of the LEND signal correlates with temperature conditions in the overlying regolith that can support water ice (see Figure 10). This does not mean that the LEND signal cannot stem from deeper layers, that is, water ice is present below the reported depths. At Cabeus crater, for which we definitely know that water ice is present, we find a good match between the areas confined by contour lines of $T = 110\text{K}$ and $\xi = 0.83$ at surface level and also at 2.25 cm depth (see Figure A6). Here, growth rates are marginal below depths of 11 cm where the overlap reaches 98.51% (see Table B2). Based on these results we find that the lateral extent of the observed LEND signal could emerge from just the upper ≈ 10 cm at Cabeus crater. We note that modeling suggests that the LCROSS impact at Cabeus crater excavated layers of dirty ice, with an ice concentration increasing with depth, down to ≈ 5.8 m below the surface (Luchsinger et al., 2021).

For the atypical NSRs at the north pole we encounter a vastly different scenario. As mentioned before the NSRs reside in non-PSR areas and their existence and development is much harder to explain. In general the suppression parameter ξ is fainter than that for the three pronounced south polar NSRs. Furthermore, there is a complete lack of correlation of the areas confined by the contour lines of $T = 110\text{K}$ and $\xi = 0.83$ at surface level, as was expected due to occasional direct illumination. For instance, the overlap of the contoured areas at surface level lie between 5.56% and 10.62% in contrast to 52.49%–100% at the south polar NSRs (see Table B2). For the NSRs near Whipple and Fibiger crater the first layer at which areas with temperatures at $T = 110\text{K}$ that visually overlap with the suppression region occur at 11 cm depth, see Figures A7c and A8c. Growth rates continue but are low toward the deepest layer at 95 cm depth (see Figure 11a). As LEND can measure down to such depths the observed signal could be explained by the existence of water ice residing between 11 and 95 cm depth. From growth rates we find that at 65 cm depth at Whipple and 35 cm depth at Fibiger crater growth ceases at overlaps of 52.55% and 67.28%, respectively. Similarly, the NSR just outside Peary crater does show some near-surface temperature patterns at 11 cm depth (Figure A9b) that could explain parts of the LEND signal but lower layers, for example, at 95 cm depth can explain the observed signal slightly better. For Peary we find that growth rates cease at a depth of 35 cm where a total overlap of 47.29% is reached. This represents the lowest percentage in overlap of all six evaluated NSRs. Although, we can show that NSRs at both poles are more likely to have ice-supporting temperatures within the upper 0.5 m of regolith compared to the average polar background (see Figure 9), the results for the north polar NSRs are not as convincing as for the ones at the south pole. For the north polar NSRs our findings are most consistent with wider (vertically) and hence deeper ranging potential ice layers than for those at the south pole, that is, upper ≈ 35 –65 cm.

Note, that we also produced temperature maps for even greater depths despite LEND's inability to detect water from deeper layers than 1 m. It was found that the emerging temperature patterns do not differ significantly from the maps at 95 cm depth and would therefore not offer a better explanation for the shape and location of the NSRs. Further we showed that growth rates for the overlap of all NSRs with cold temperature layers cease above 1 m depth (see Table B2).

Although both central polar regions offer large areas with temperatures below 110 K we find no significant neutron suppression and hence no sign for water ice (see Figures A2 and A3).

4. Discussion

The co-evaluation of LEND's suppression parameters with temperature clearly supports the existence of (near)-surface water ice at our selected south polar NSRs. Here, the "classical" theory of how wet PSRs come into existence seems to hold; water molecules migrate via ballistic hops (Butler, 1997; Butler et al., 1993) from anywhere on the lunar surface toward the poles and accumulate on the cold surfaces within PSRs (Watson et al., 1961). From growth rates in Figure 11, we conclude that ice at the NSRs of Shoemaker and Cabeus could already be concentrated within the upper 4 cm after which growth rates sharply decrease and

cease at 19 cm. At Cabeus crater we find that the areal overlap at which hydrogen is observed by LEND and ice can be stable with respect to temperature grows by 30% within the upper most 2 cm of regolith (see Figure 11 and Table B2). The NSR within the PSR of Haworth crater suggests water ice could be present at surface level.

For our north polar NSRs the accumulation mechanism seems to differ from the south polar NSRs since here surface temperatures are too high for water ice to become trapped. We further note that parts of all our selected north polar NSRs reside on relatively warmer equator-facing slopes at which generally no water ice is found (Rubanenko et al., 2019). At those sloped surfaces, the histogram, defined by our neutron suppression threshold (see left Figure 9), shows a significant amount of depths at which ice could be stable and are deeper than 1 m. Here, LEND should report no suppression at all. However, since the north polar NSRs reside in and near well illuminated and warm regions the reported depths to temperatures where ice can be stable can be attributed to the limited resolution and imperfect overlap of both maps, the neutron suppression as well the depth-to-ice map. In spite of everything, LEND shows a clear sign of hydrogen at those sites and we could show with this study that temperatures in the near sub-surface are such that water ice can be stable. One plausible scenario would be that water molecules at those locations are efficiently buried. In accordance we find that growth rates remain active to greater depths than at the south polar NSRs (see Figure 11). Interestingly, growth rates also decrease beyond a similar depth as reported for the south pole, that is, 4 cm, suggesting that favorable temperatures for water ice are generally already found within the top few centimeters. However, the decrease in growth rates is significantly slower than at the south pole and growth continues to depths of up to 65 cm. In fact, Schorghofer and Aharonson (2014) found that water molecules can be pumped down into the sub-surface by diurnal temperature cycles under very specific circumstances. They found that ideal conditions for pumping emerge if the mean surface temperature is below 105 K and the maximum surface temperature is above 120 K. Although they report that such temperature regimes are commonly found on pole-facing slopes they also found that within a few degrees of the poles pumping is actually preferred on equator-facing slopes. As stated before, our selected north polar NSRs all reside on equator-facing slopes within a few degrees of the poles and we find that $\approx 40\%$ – 60% of the surface area confined by the suppression parameter ($\xi \leq 0.83$) do indeed offer such ideal pumping conditions. Since the areas where ice pumping occurs complement the areas where water ice can be stable at surface level, that is, the areas do not overlap, the total surface area of the NSRs for which we can either find stable water ice or find ice pumping amounts to $\approx 45\%$ – 70% at surface level. Those numbers are found again at 65 cm depth where we defined the minimum deposit depth for water ice by ceasing growth rates (compare to Table B2). Note that the ice pump is inactive below ≈ 20 cm and lower layers of ice need to subsequently be buried by a different mechanism, for example, mass wasting events and impact gardening (e.g., Horz & Cintala, 1997).

We note that this mechanism is also active at the south polar NSRs at the smaller fractions where the NSRs are occasionally in sunlight, for example, Shoemaker and Cabeus crater (see Figures A4 and A6). Here the total percentage of NSR overlap at the surface, either with temperature or ice pumping, amounts to $\approx 98\%$ – 100% . Similarly, percentages are again found at our defined minimum deposit depths for water ice (compare percentages given in bold in Table B2).

The fact that our temperature maps have a resolution of 200 m and LEND's suppression parameters are reported in oddly shaped pixels of 0.501° in longitude (≈ 7.75 km at 89°) and 0.0625° in latitude (≈ 15 km), leads to inevitable resampling effects. Since we used a straight-forward approach in determining overlap by simply overlaying our two maps and reporting the common area, we tend to underestimate the actual overlap since our determining factor is the higher resolved temperature map.

5. Conclusion

This study confirms previous observations that temperature alone is not a sufficient predictor of the distribution of ice deposits. For instance, we showed that water ice locations predicted solely by maximum temperature within the upper 1 m of regolith do not always coincide with NSRs identified by LEND, insinuating that maximum temperature might not be the only or main driver for the accumulation of water ice. Furthermore, we report on two populations of NSRs which significantly differ in the locations where they are found. Our selected south polar NSRs all follow the “classical” view that water ice only accumulates in the

cold, polar PSRs. Our selected north polar NSRs drastically differ in that none of them are found in a PSR. Although we can show that their existence can be described by ice pumping and subsequent accumulation at cold layers in the sub-surface, it is unclear why the NSRs with the most expressed suppression in the polar regions differ in such way. From the eight reported NSRs in the south polar region by Sanin et al. (2017) we find that that are classical NSRs (Cabeus, Shoemaker, and Haworth), one needed to be excluded due to lack of data (Hale Q) and four are atypical NSRs (Amundsen, Idel'son L, deGerlache. and Scott M). However, three of the four atypical NSRs (Amundsen, Idel'son L, and deGerlache) have less pronounced suppression and do not meet our criteria of $\xi \leq 0.83$. Out of the seven reported north polar NSRs by Sanin et al. (2017) we find four atypical NSRs (Peary, Fibiger, Whipple, and an unnamed crater) which all meet our criteria, that is, we consider them to have "Cabeus-like" suppression and hence assume they contain water ice. Furthermore, we find two north polar NSRs (Plaskett and Rozhdenstvenskiy) which are classical and one NSR that was excluded due to the lack of data (Milankovic E).

It is noticeable that the deepest suppressions at the south pole occur in classical NSRs where at the north pole they occur in atypical NSRs, yet we also find NSRs from the other population at each pole as well. Hence, in our study, we cannot observe a trend for one population being more prominent at one of the poles. However, from our investigation we can conclude that the accumulation process for water ice in the classical and the atypical NSRs is driven by different processes. In the classical NSRs, where surface temperatures are cold enough, water ice can accumulate directly at the surface. Water ice located in deeper layers is most likely buried by impact gardening since temperatures in classical NSRs are such that ice pumping is not an effective burial process. In the atypical NSRs, however, water ice seems to be buried efficiently by ice pumping with other burial processes acting subsequently, for example, impact gardening and mass wasting events. Although our investigation cannot pinpoint to the source of delivery we suspect that the presence of hydrogen in just some of the polar PSRs in conjunction with the existence of wet non-PSR regions seems to stem from an unconnected and local rather than an ubiquitous and global process since the thermal environment is comparable in all polar PSRs (Costello et al., 2020; Honniball et al., 2020). For instance, if polewards hopping of water molecules were the most prominent water delivery process then we would expect most PSRs to have elevated hydrogen abundances. Since this is not the case and there is no known mechanism that would prefer certain pathways for the poleward hopping with subsequent deposition in specific areas, that is, the NSRs, we suspect other processes must be responsible. A similar argument can be made for hydrogen delivery by solar wind and degassing from the lunar interior. It seems unlikely that those globally acting processes are independently responsible for the enhanced hydrogen abundance in the observed NSRs. For instance, compare the two south polar PSRs Shackleton and Shoemaker in Figure 8, and in Figures A2 and A4. Despite the fact that they are in direct vicinity, Shackleton shows no distinct sign for hydrogen. Modeling results from Cannon et al. (2020) show similar results and suggest that the relatively younger age of Shackleton could be the reason for the lack of significant water ice.

Although aforementioned processes most certainly contribute to observe polar hydrogen abundance in general, as can be clearly seen by the fuzzy region of hydrogen abundance in Figure 8, we suspect that local asteroidal and cometary impacts are most likely the source of delivery to the regions with distinctively larger hydrogen abundance. This finding agrees with modeling results in the study by Cannon et al. (2020). Here, we suggest that possible impactors mainly contribute to the immediate vicinity of the impact site for the same reasons as stated above; nearby PSRs would otherwise show enhanced hydrogen signals as well.

Our study shows that temperature alone cannot point to water ice reservoirs but is an essential pre-condition for the accumulation of water ice and always needs to be evaluated to support other observations, for example, LEND. In conclusion we could show that the six NSRs investigated in this study coincide with temperature maps which allow for water ice or ice pumping, either at surface level or within the first meter of regolith.

Finally, we want to mention again that LEND data is challenged by some authors (e.g., Eke et al., 2012; Lawrence et al., 2011; Teodoro et al., 2014) and, that at this time, there is no data available to cross-validate the results of this study at resolutions similar to that of the LEND instrument. Future, high-resolution neutron spectrometers will therefore be essential to support or disprove findings made based on LEND data.

Appendix A

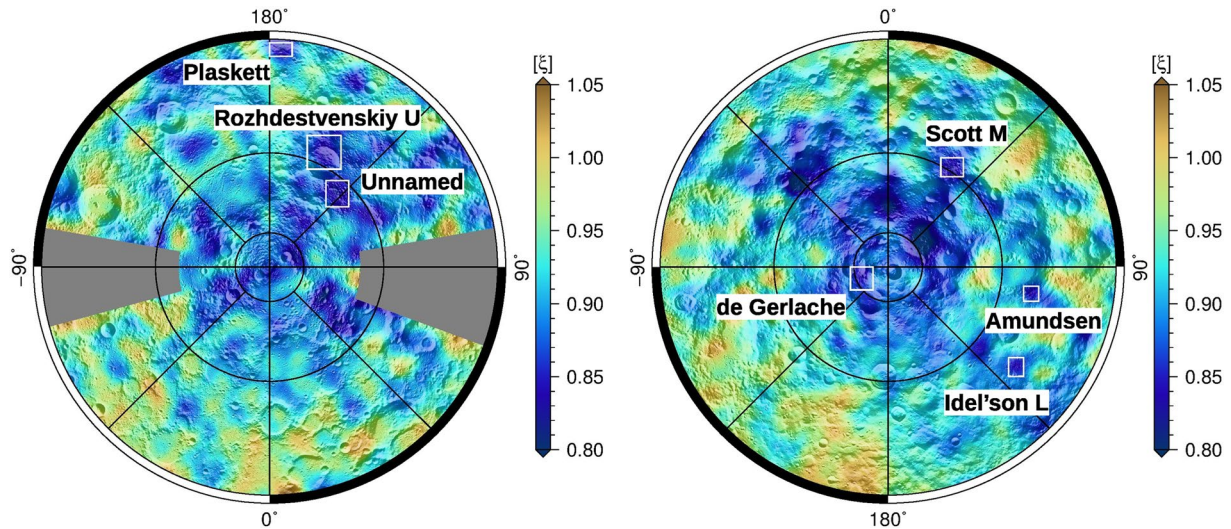


Figure A1. Maps of suppression parameter ξ derived from neutron counts measured by Lunar Exploration Neutron Detector. Neutron suppressed regions (NSRs) which are not further discussed in the study are shown within white boxes. (Left) North polar map of ξ with the two classical NSRs Plaskett and Rozhdstvenskiy and the atypical and unnamed NSR. The gray areas are left out due to poor statics of neutron measurements in these regions (see Sanin et al. (2017)). (Right) South polar map of ξ with the four atypical NSRs deGerlache, Scott M, Amundsen, and Idel'son L. Milankovic E at the north and Hale Q at the south pole are outside our map range and were excluded.

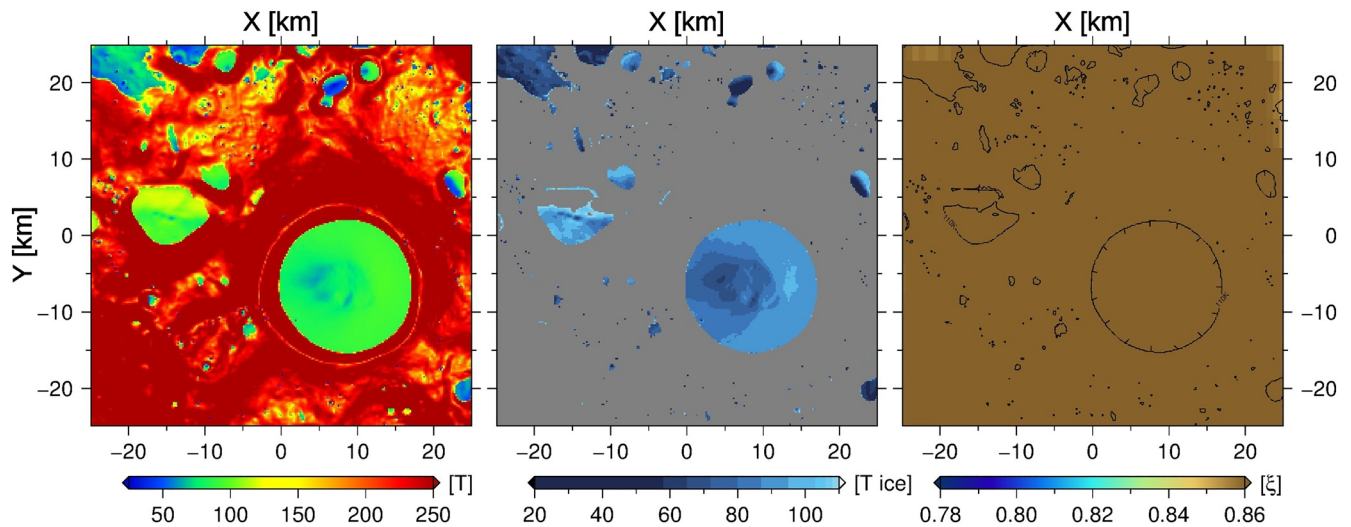


Figure A2. Central south polar regions of interest. (Left) Maximum temperature. (Middle) Possible locations for water ice ($T \leq 110$ K) and (right) Lunar Exploration Neutron Detector neutron suppression parameter map at surface level. The areas where $T \leq 110$ K are contoured in black, however, no significant neutron suppression can be found (i.e., $\xi > 0.83$).

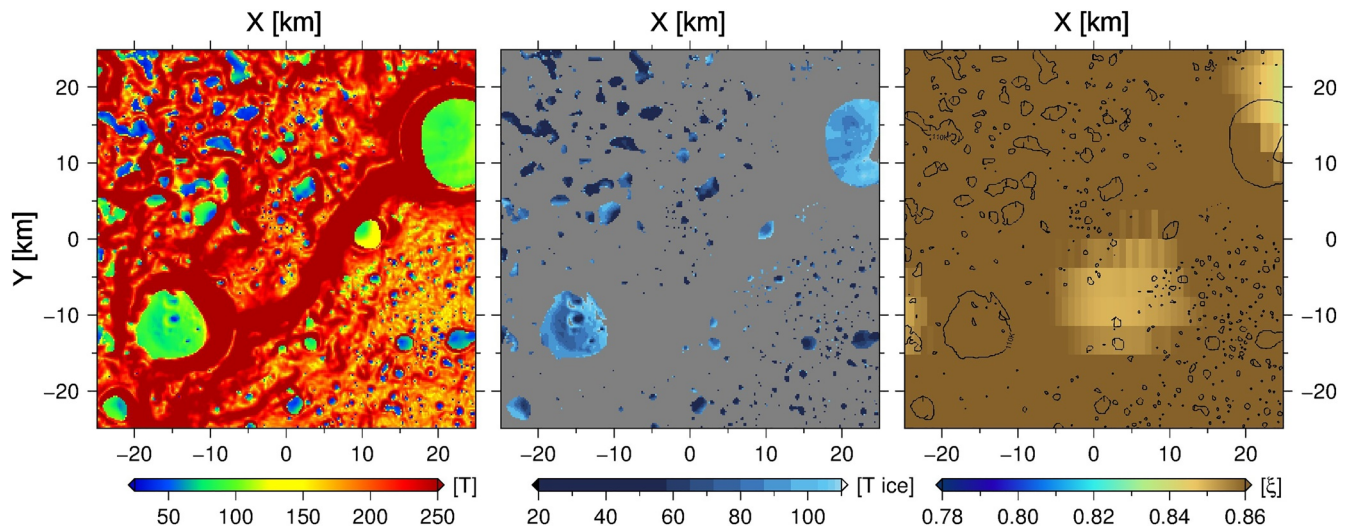


Figure A3. Central north polar regions of interest. (Left) Maximum temperature. (Middle) Possible locations for water ice ($T \leq 110$ K) and (right) Lunar Exploration Neutron Detector neutron suppression parameter map at surface level. The areas where $T \leq 110$ K are contoured in black, however, no significant neutron suppression can be found (i.e., $\xi > 0.83$).

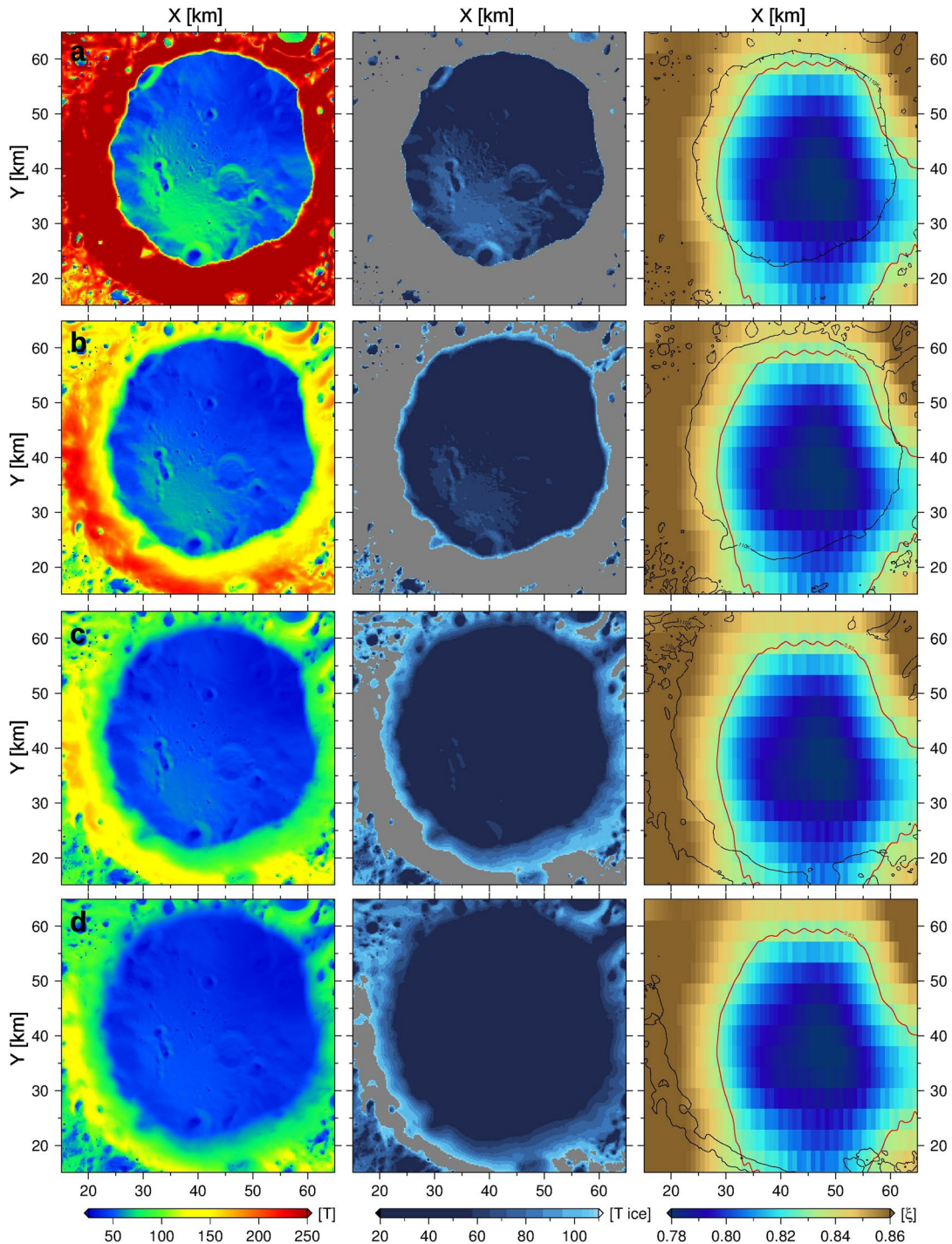


Figure A4. South polar crater Shoemaker. (Left) Maximum temperature. (Middle) Possible locations for water ice ($T \leq 110$ K) and (right) Lunar Exploration Neutron Detector neutron suppression parameter map at (a) surface level, (b) 2.25 cm, (c) 11 cm, and (d) 95 cm. The areas where $T \leq 110$ K and $\xi \leq 0.83$ are contoured in black and red, respectively.

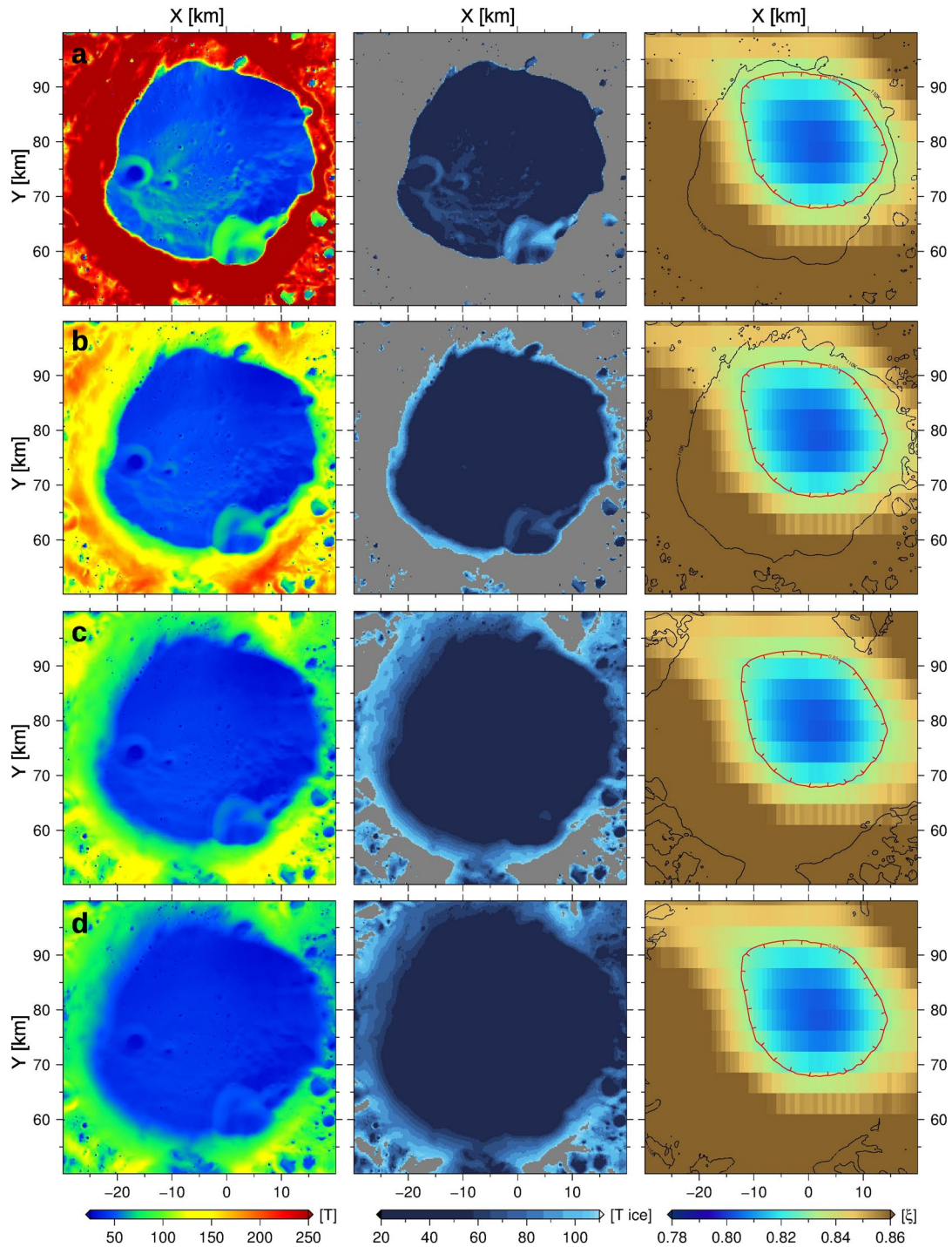


Figure A5. South polar crater Haworth. (Left) Maximum temperature. (Middle) Possible locations for water ice ($T \leq 110$ K) and (right) Lunar Exploration Neutron Detector neutron suppression parameter map at (a) surface level, (b) 2.25 cm, (c) 11 cm, and (d) 95 cm. The areas where $T \leq 110$ K and $\xi \leq 0.83$ are contoured in black and red, respectively.

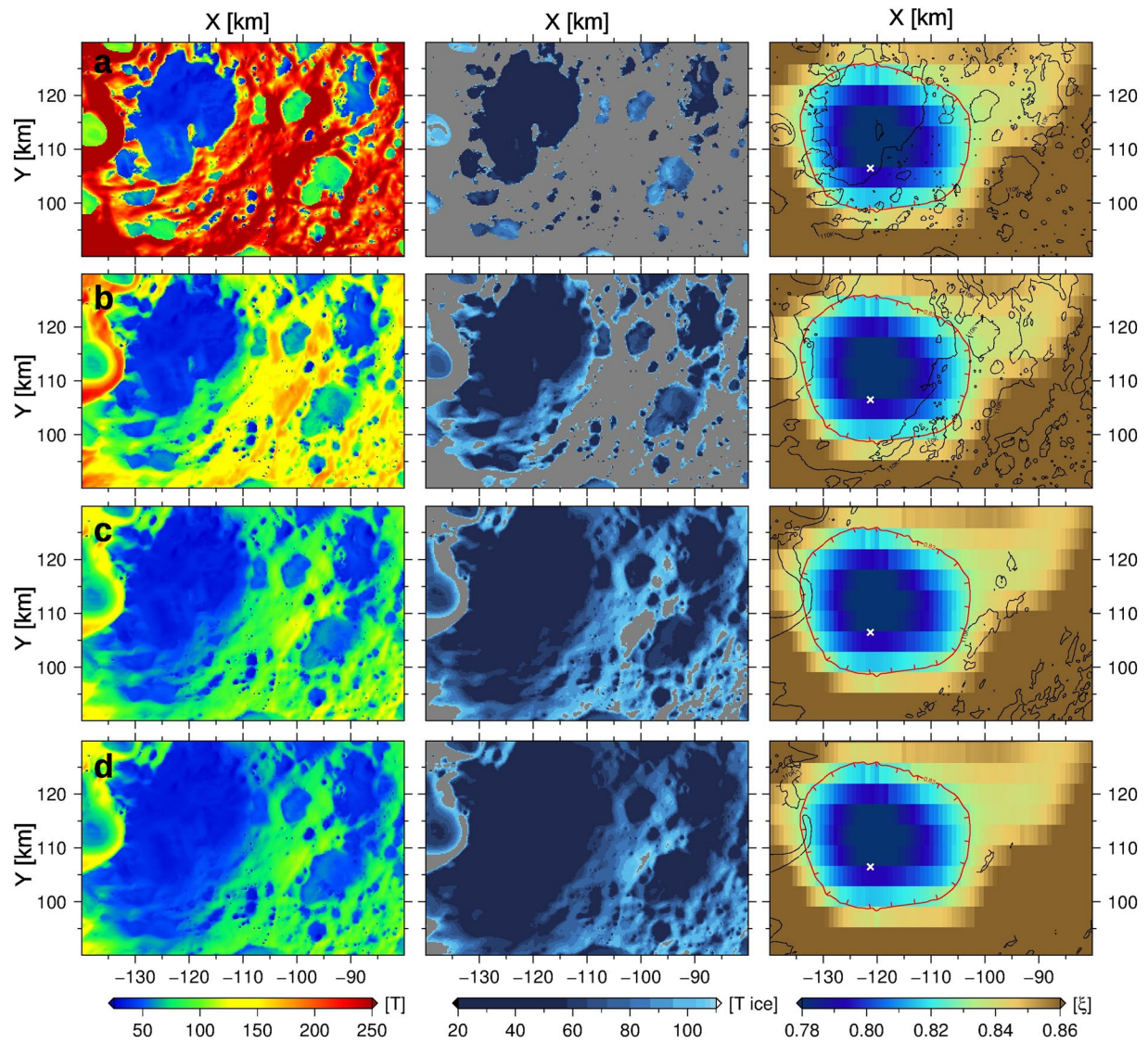


Figure A6. South polar crater Cabeus. The LCROSS impact site is indicated by a white cross. (Left) Maximum temperature. (Middle) Possible locations for water ice ($T \leq 110$ K) and (right) LEND neutron suppression parameter map at (a) surface level, (b) 2.25 cm, (c) 11 cm, and (d) 95 cm. The areas where $T \leq 110$ K and $\xi \leq 0.83$ are contoured in black and red, respectively.

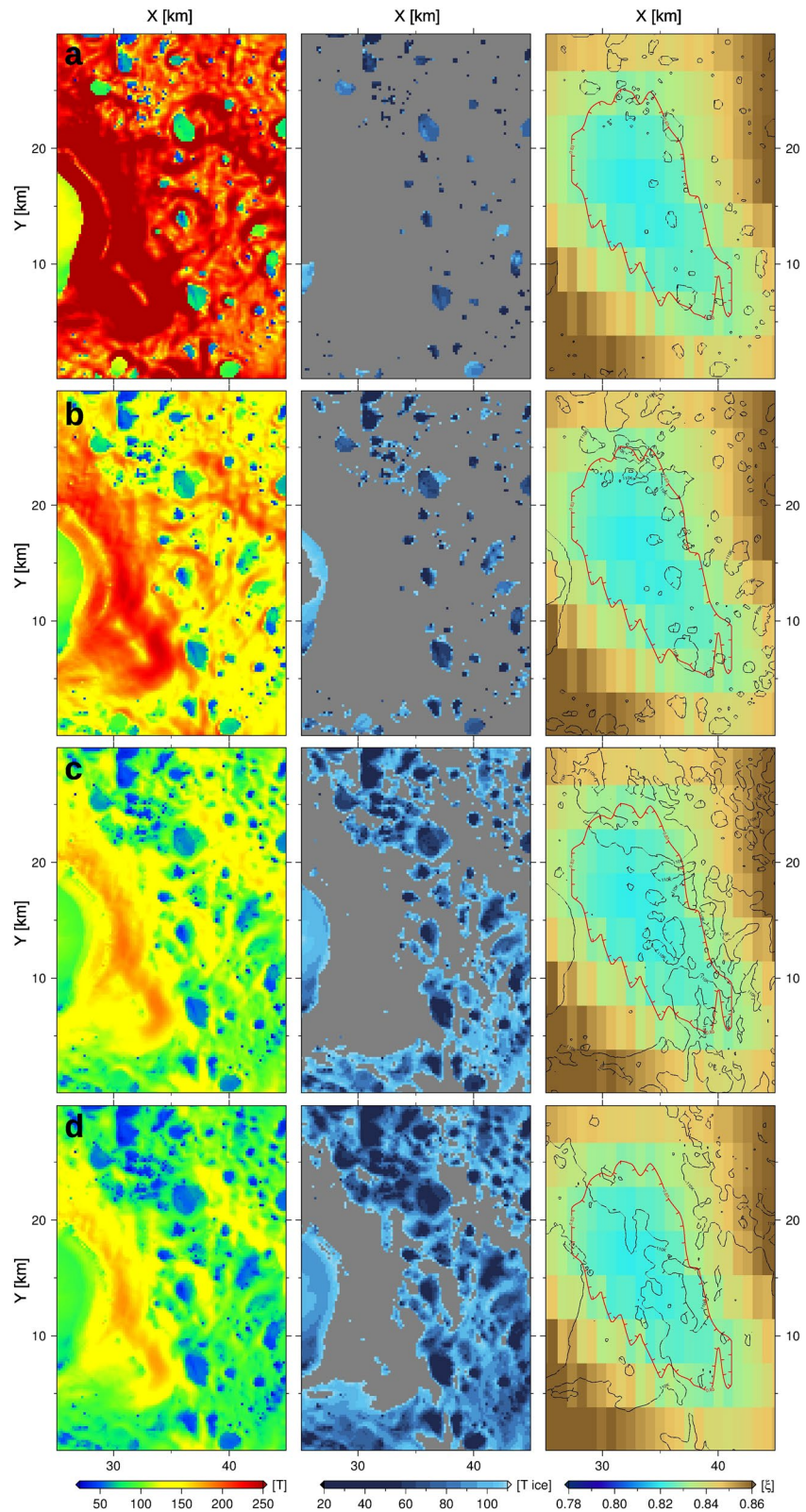


Figure A7. Area outside north polar crater Whipple. (Left) Maximum temperature. (Middle) Possible locations for water ice ($T \leq 110$ K) and (right) LEND neutron suppression parameter map at (a) surface level, (b) 2.25 cm, (c) 11 cm, and (d) 95 cm. The areas where $T \leq 110$ K and $\xi \leq 0.83$ are contoured in black and red, respectively.

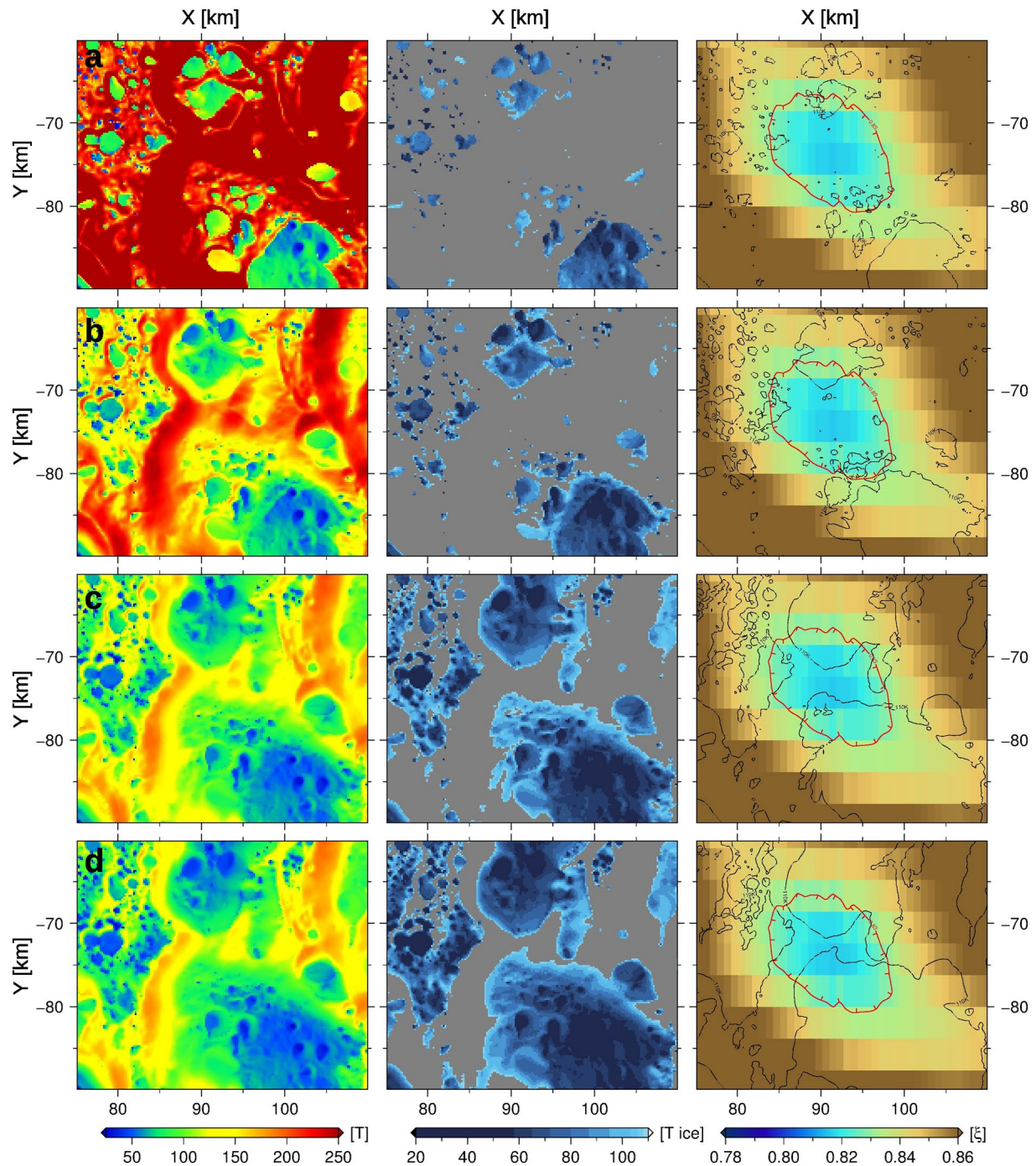


Figure A8. Area outside north polar crater Fibiger. (Left) Maximum temperature. (Middle) Possible locations for water ice ($T \leq 110$ K) and (right) LEND neutron suppression parameter map at (a) surface level, (b) 2.25 cm, (c) 11 cm, and (d) 95 cm. The areas where $T \leq 110$ K and $\xi \leq 0.83$ are contoured in black and red, respectively.

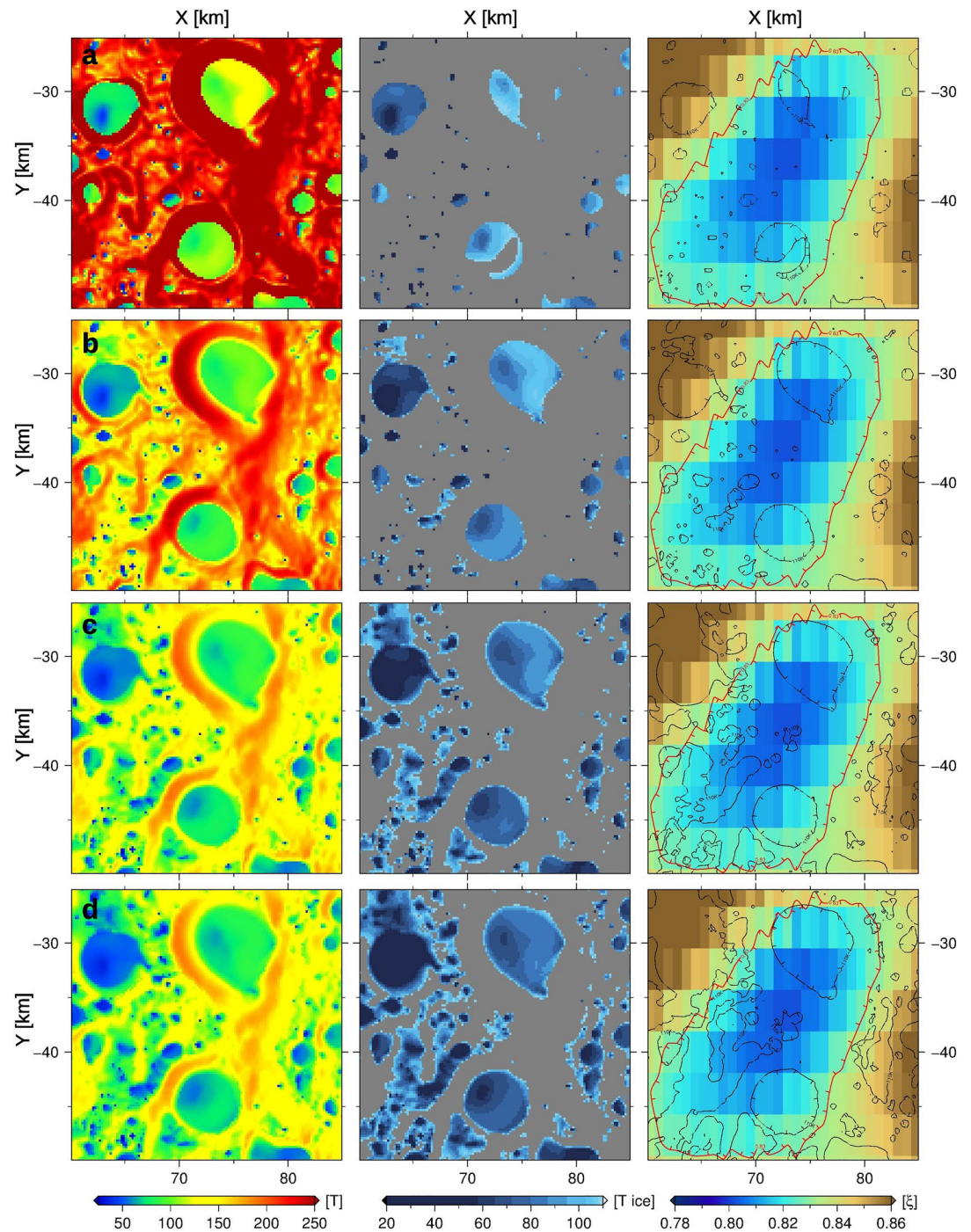


Figure A9. Area outside north polar crater Peary. (Left) Maximum temperature. (Middle) Possible locations for water ice ($T \leq 110$ K) and (right) LEND neutron suppression parameter map at (a) surface level, (b) 2.25 cm, (c) 11 cm, and (d) 95 cm. The areas where $T \leq 110$ K and $\xi \leq 0.83$ are contoured in black and red, respectively.

Appendix B

Table B1

The Minimum, Average and Maximum Temperature as a Function of Depth for the Eight Polar Regions of Interests

RoI	T (K)			
	Surface	2.25 cm	11 cm	185 cm
	Min/Avg/Max	Min/Avg/Max	Min/Avg/Max	Min/Avg/Max
SP—central	23.35/184.18/339.07	23.59/187.39/261.20	23.91/187.82/203.66	27.91/191.66/191.77
SP—Haworth	23.35/182.85/320.82	23.59/193.80/253.88	23.91/194.81/206.88	27.91/198.62/198.65
SP—Cabeus	23.35/188.70/330.89	23.59/200.97/262.02	23.91/202.10/212.77	27.91/205.89/205.92
SP—Shoemaker	23.35/184.10/338.26	23.59/188.02/260.89	23.91/189.06/203.24	27.91/192.89/192.93
NP—central	23.35/189.35/330.46	23.59/192.38/255.71	23.91/192.86/204.20	27.91/196.70/196.88
NP—Peary	23.35/180.48/327.22	23.59/192.38/256.75	23.91/193.44/204.43	27.91/197.25/197.32
NP—Fibiger	23.35/183.54/333.72	23.59/195.18/260.61	23.91/196.30/206.47	27.91/200.08/200.13
NP—Whipple	23.35/189.34/330.94	23.59/192.38/256.63	23.91/192.86/204.20	27.91/196.69/196.88

Table B2

Overlap of LEND Suppression Regions of $\xi \leq 0.83$ and Areas With Temperatures $T \leq 110$ K Given in Percentages

Depth (cm)	Overlap in % of NSRs with cold layers ($T \leq 110$ K) at					
	South pole			North pole		
	Shoemaker	Haworth	Cabeus	Whipple	Fibiger	Peary
0.0000	72.40	100.00	52.49	5.56	10.62	9.88
0.2500	72.73	100.00	54.99	5.82	11.67	12.56
0.7500	73.59	100.00	63.76	6.71	13.68	14.42
1.2500	74.49	100.00	71.95	8.20	15.67	17.79
1.7500	75.43	100.00	78.40	9.73	17.75	21.03
2.2500	76.43	100.00	81.27	11.05	20.15	22.42
2.7500	77.63	100.00	83.28	12.62	23.14	23.61
3.2500	79.26	100.00	85.19	14.35	26.90	24.86
3.7500	81.58	100.00	86.91	16.41	30.87	26.22
4.2500	83.56	100.00	88.99	18.19	34.55	27.73
4.7500	85.45	100.00	91.33	19.99	38.06	28.95
5.5000	87.46	100.00	94.05	22.66	41.95	30.45
6.5000	89.58	100.00	96.28	25.53	46.71	32.45
7.5000	91.45	100.00	97.02	28.14	50.58	34.03
8.5000	92.75	100.00	97.74	30.18	53.41	35.56
9.5000	93.42	100.00	98.33	31.80	55.78	36.92
11.0000	94.10	100.00	98.51	33.91	58.21	38.83
13.0000	94.65	100.00	98.57	37.01	60.14	40.48
15.0000	95.03	100.00	98.68	39.65	61.81	41.85
17.0000	95.32	100.00	98.73	41.30	63.13	42.76

Table B2
Continued

Depth (cm)	Overlap in % of NSRs with cold layers ($T \leq 110$ K) at					
	South pole			North pole		
	Shoemaker	Haworth	Cabeus	Whipple	Fibiger	Peary
19.0000	95.56	100.00	98.82	42.88	63.95	43.74
22.5000	95.90	100.00	98.86	44.91	65.24	44.97
27.5000	96.34	100.00	98.88	46.81	66.17	46.11
35.0000	96.79	100.00	98.91	48.62	67.28	47.29
45.0000	97.19	100.00	98.96	50.09	67.97	48.00
65.0000	97.74	100.00	99.03	52.55	69.03	48.89
95.0000	98.05	100.00	99.04	53.09	69.13	49.01

Note. For the south polar NSRs growth rates cease ($g < 0.1\%/cm$) within the upper 19 cm. At the north polar NSRs growth rates continue up to depths of 65 cm, that is, at least three-times deeper than at the south polar NSRs. The depths at which growth rates cease at each site are presented in bold.

Data Availability Statement

LRO data can be accessed online via the NASA Planetary Data System (PDS) at <https://pds-geosciences.wustl.edu/missions/lro/>. The data to reproduce figures and results presented in this study can be accessed online at Gläser (2020).

Acknowledgments

P. Gläser was funded by a Grant of the German Research Foundation (GL 865/2-1). The authors gratefully acknowledge the support of NVIDIA Corporation with the donation of a Quadro P6000 GPU used for this research. The authors would also wish to thank the Lunar Reconnaissance Orbiter (LRO) Science Teams for releasing such wonderful data products. Open access funding enabled and organized by Projekt DEAL.

References

- Arnold, J. R. (1979). Ice in the lunar polar regions. *Journal of Geophysical Research*, *84*, 5659–5668. <https://doi.org/10.1029/JB084iB10p05659>
- Benna, M., Hurley, D. M., Stubbs, T. J., Mahaffy, P. R., & Elphic, R. C. (2019). Lunar soil hydration constrained by exospheric water liberated by meteoroid impacts. *Nature Geoscience*, *12*(5), 333–338. <https://doi.org/10.1038/s41561-019-0345-3>
- Boynton, W. V., Droege, G. F., Mitrofanov, I. G., McClanahan, T. P., Sanin, A. B., Litvak, M. L., et al. (2012). High spatial resolution studies of epithermal neutron emission from the lunar poles: Constraints on hydrogen mobility. *Journal of Geophysical Research*, *117*, E00H33. <https://doi.org/10.1029/2011JE003979>
- Bussey, D. B. J., McGovern, J. A., Spudis, P. D., Neish, C. D., Noda, H., Ishihara, Y., & Sørensen, S.-A. (2010). Illumination conditions of the south pole of the Moon derived using Kaguya topography. *Icarus*, *208*, 558–564. <https://doi.org/10.1016/j.icarus.2010.03.028>
- Butler, B. J. (1997). The migration of volatiles on the surfaces of Mercury and the Moon. *Journal of Geophysical Research*, *102*(E8), 19283–19291. <https://doi.org/10.1029/97JE01347>
- Butler, B. J., Muhleman, D. O., & Slade, M. A. (1993). Mercury: Full-disk radar images and the detection and stability of ice at the north pole. *Journal of Geophysical Research*, *98*(E8), 15003–15023. <https://doi.org/10.1029/93je01581>
- Cannon, K. M., Deutsch, A. N., Head, J. W., & Britt, D. T. (2020). Stratigraphy of ice and ejecta deposits at the lunar poles. *Geophysical Research Letters*, *47*(21), e88920. <https://doi.org/10.1029/2020GL088920>
- Clark, R. N. (2009). Detection of adsorbed water and hydroxyl on the Moon. *Science*, *326*(5952), 562–564. <https://doi.org/10.1126/science.1178105>
- Colaprete, A., Schultz, P., Heldmann, J., Wooden, D., Shirley, M., Ennico, K., et al. (2010). Detection of water in the LCROSS ejecta plume. *Science*, *330*(6003), 463–468. <https://doi.org/10.1126/science.1186986>
- Costello, E. S., Ghent, R. R., Hirabayashi, M., & Lucey, P. G. (2020). Impact gardening as a constraint on the age, source, and evolution of ice on Mercury and the Moon. *Journal of Geophysical Research*, *125*(3), e06172. <https://doi.org/10.1029/2019JE006172>
- Crider, D., & Vondrak, R. (2002). Hydrogen migration to the lunar poles by solar wind bombardment of the moon. *Advances in Space Research*, *30*(8), 1869–1874. [https://doi.org/10.1016/s0273-1177\(02\)00493-3](https://doi.org/10.1016/s0273-1177(02)00493-3)
- Eke, V. R., Bartram, S. A., Lane, D. A., Smith, D., & Teodoro, L. F. A. (2014). Lunar polar craters—icy, rough or just sloping? *Icarus*, *241*, 66–78. <https://doi.org/10.1016/j.icarus.2014.06.021>
- Eke, V. R., Teodoro, L. F. A., & Elphic, R. C. (2009). The spatial distribution of polar hydrogen deposits on the Moon. *Icarus*, *200*(1), 12–18. <https://doi.org/10.1016/j.icarus.2008.10.013>
- Eke, V. R., Teodoro, L. F. A., Lawrence, D. J., Elphic, R. C., & Feldman, W. C. (2012). A quantitative comparison of lunar orbital neutron data. *The Astrophysical Journal*, *747*(1), 6. <https://doi.org/10.1088/0004-637x/747/1/6>
- Farrell, W. M., Hurley, D. M., Poston, M. J., Hayne, P. O., Szalay, J. R., & McLain, J. L. (2019). The young age of the LAMP-observed frost in lunar polar cold traps. *Geophysical Research Letters*, *46*(15), 8680–8688. <https://doi.org/10.1029/2019GL083158>
- Feldman, W. C., Maurice, S., Binder, A. B., Barraclough, B. L., Elphic, R. C., & Lawrence, D. J. (1998). Fluxes of fast and epithermal neutrons from lunar prospector: Evidence for water ice at the lunar poles. *Science*, *281*, 1496–1500. <https://doi.org/10.1126/science.281.5382.1496>
- Fisher, E. A., Lucey, P. G., Lemelin, M., Greenhagen, B. T., Siegler, M. A., Mazarico, E., et al. (2017). Evidence for surface water ice in the lunar polar regions using reflectance measurements from the Lunar Orbiter Laser Altimeter and temperature measurements from the diviner lunar radiometer experiment. *Icarus*, *292*, 74–85. <https://doi.org/10.1016/j.icarus.2017.03.023>

- Gläser, P. (2020). *Temperatures near the lunar poles and their correlation with hydrogen predicted by LEND*. <https://doi.org/10.14279/depositonce-10363.2>
- Gläser, P., & Gläser, D. (2019). Modeling near-surface temperatures of airless bodies with application to the Moon. *Astronomy & Astrophysics*, 627, A129. <https://doi.org/10.1051/0004-6361/201935514>
- Gläser, P., Haase, I., Oberst, J., & Neumann, G. A. (2013). Co-registration of laser altimeter tracks with digital terrain models and applications in planetary science. *Planetary and Space Science*, 89, 111–117. <https://doi.org/10.1016/j.pss.2013.09.012>
- Gläser, P., Oberst, J., Neumann, G. A., Mazarico, E., Speyerer, E. J., & Robinson, M. S. (2018). Illumination conditions at the lunar poles: Implications for future exploration. *Planetary and Space Science*, 162, 170–178. <https://doi.org/10.1016/j.pss.2017.07.006>
- Gläser, P., Scholten, F., De Rosa, D., Marco Figueroa, R., Oberst, J., Mazarico, E., et al. (2014). Illumination conditions at the lunar south pole using high resolution Digital Terrain Models from LOLA. *Icarus*, 243, 78–90. <https://doi.org/10.1016/j.icarus.2014.08.013>
- Harmon, J. K. (2007). Radar imaging of Mercury. *Space Science Reviews*, 132(2–4), 307–349. <https://doi.org/10.1007/s11214-007-9234-y>
- Haruyama, J., Ohtake, M., Matsunaga, T., Morota, T., Honda, C., Yokota, Y., et al. (2008). Lack of exposed ice inside lunar south pole Shackleton crater. *Science*, 322(5903), 938–939. <https://doi.org/10.1126/science.1164020>
- Haruyama, J., Yamamoto, S., Yokota, Y., Ohtake, M., & Matsunaga, T. (2013). An explanation of bright areas inside Shackleton Crater at the Lunar South Pole other than water-ice deposits. *Geophysical Research Letters*, 40(15), 3814–3818. <https://doi.org/10.1002/grl.50753>
- Hayne, P. O., Aharonson, O., & Schörghofer, N. (2020). Micro cold traps on the Moon. *Nature Astronomy*, 5, 169–175. <https://doi.org/10.1038/s41550-020-1198-9>
- Hayne, P. O., Hendrix, A., Sefton-Nash, E., Siegler, M. A., Lucey, P. G., Retherford, K. D., et al. (2015). Evidence for exposed water ice in the Moon's south polar regions from Lunar Reconnaissance Orbiter ultraviolet albedo and temperature measurements. *Icarus*, 255, 58–69. <https://doi.org/10.1016/j.icarus.2015.03.032>
- Head, J. W., Wilson, L., Deutsch, A. N., Rutherford, M. J., & Saal, A. E. (2020). Volcanically induced transient atmospheres on the Moon: Assessment of duration, significance, and contributions to polar volatile traps. *Geophysical Research Letters*, 47(18), e89509. <https://doi.org/10.1029/2020GL089509>
- Hemingway, B. S., Robie, R. A., & Wilson, W. H. (1973). Specific heats of lunar soils, basalt, and breccias from the Apollo 14, 15, and 16 landing sites, between 90 and 350 K. *Lunar and Planetary Science Conference Proceedings*, 4, 2481.
- Honniball, C. I., Lucey, P. G., Li, S., Shenoy, S., Orlando, T. M., Hibbitts, C. A., et al. (2020). Molecular water detected on the sunlit Moon by SOFIA. *Nature Astronomy*, 5, 121–127. <https://doi.org/10.1038/s41550-020-01222-x>
- Horz, F., & Cintala, M. (1997). Impact experiments related to the evolution of planetary regoliths. *Meteoritics and Planetary Science*, 32, 179–209. <https://doi.org/10.1111/j.1945-5100.1997.tb01259.x>
- Hurley, D. M., Lawrence, D. J., Bussey, D. B. J., Vondrak, R. R., Elphic, R. C., & Gladstone, G. R. A. (2012). Two-dimensional distribution of volatiles in the lunar regolith from space weathering simulations. *Geophysical Research Letters*, 39(9), L09203. <https://doi.org/10.1029/2012GL051105>
- Killen, R. M., Benkhoff, J., & Morgan, T. H. (1997). Mercury's polar caps and the generation of an OH exosphere. *Icarus*, 125(1), 195–211. <https://doi.org/10.1006/icar.1996.5601>
- Langseth, M. G., Keihm, S. J., & Peters, K. (1976). Revised lunar heat-flow values. *Lunar and Planetary Science Conference Proceedings*, 3, 3143–3171.
- Lawrence, D. J. (2017). A tale of two poles: Toward understanding the presence, distribution, and origin of volatiles at the polar regions of the Moon and Mercury. *Journal of Geophysical Research: Planets*, 122(1), 21–52. <https://doi.org/10.1002/2016JE005167>
- Lawrence, D. J., Eke, V. R., Elphic, R. C., Feldman, W. C., Funsten, H. O., Prettyman, T. H., & Teodoro, L. F. A. (2011). Technical comment on “hydrogen mapping of the lunar south pole using the LRO neutron detector experiment LEND”. *Science*, 334(6059), 1058. <https://doi.org/10.1126/science.1203341>
- Li, S., Lucey, P. G., Milliken, R. E., Hayne, P. O., Fisher, E., Williams, J.-P., et al. (2018). Direct evidence of surface exposed water ice in the lunar polar regions. *Proceedings of the National Academy of Science of the United States of America*, 115(36), 8907–8912. <https://doi.org/10.1073/pnas.1802345115>
- Litvak, M. L., Mitrofanov, I. G., Sanin, A., Malakhov, A., Boynton, W. V., Chin, G., & Zuber, M. T. (2012). Global maps of lunar neutron fluxes from the lend instrument. *Journal of Geophysical Research*, 117(E12). <https://doi.org/10.1029/2011je003949>
- Litvak, M. L., Mitrofanov, I. G., Sanin, A. B., Bakhtin, B. N., Bodnarik, J. G., Boynton, W. V., et al. (2016). The variations of neutron component of lunar radiation background from LEND/LRO observations. *Planetary and Space Science*, 122, 53–65. <https://doi.org/10.1016/j.pss.2016.01.006>
- Livengood, T. A., Mitrofanov, I. G., Chin, G., Boynton, W. V., Bodnarik, J. G., Evans, L. G., et al. (2018). Background and lunar neutron populations detected by LEND and average concentration of near-surface hydrogen near the Moon's poles. *Planetary and Space Science*, 162, 89–104. <https://doi.org/10.1016/j.pss.2017.12.004>
- Luchsinger, K. M., Chanover, N. J., & Strycker, P. D. (2021). Water within a permanently shadowed lunar crater: Further LCROSS modeling and analysis. *Icarus*, 354, 114089. <https://doi.org/10.1016/j.icarus.2020.114089>
- Marshall, W., Shirley, M., Moratto, Z., Colaprete, A., Neumann, G., Smith, D., et al. (2011). Locating the LCROSS impact craters. *Space Science Reviews*, 167(1–4), 71–92. <https://doi.org/10.1007/s11214-011-9765-0>
- Mazarico, E., Neumann, G. A., Smith, D. E., Zuber, M. T., & Torrence, M. H. (2011). Illumination conditions of the lunar polar regions using LOLA topography. *Icarus*, 211, 1066–1081. <https://doi.org/10.1016/j.icarus.2010.10.030>
- Miller, R. S., Lawrence, D. J., & Hurley, D. M. (2014). Identification of surface hydrogen enhancements within the Moon's Shackleton crater. *Icarus*, 233, 229–232. <https://doi.org/10.1016/j.icarus.2014.02.007>
- Mitrofanov, I., Litvak, M., Sanin, A., Malakhov, A., Golovin, D., Boynton, W., et al. (2012). Testing polar spots of water-rich permafrost on the Moon: LEND observations onboard LRO. *Journal of Geophysical Research*, 117, E00H27. <https://doi.org/10.1029/2011je003956>
- Mitrofanov, I., Sanin, A. B., Boynton, W. V., Chin, G., Garvin, J. B., Golovin, D., et al. (2010). Hydrogen mapping of the lunar south pole using the LRO neutron detector experiment LEND. *Science*, 330(6003), 483–486. <https://doi.org/10.1126/science.1185696>
- Mitrofanov, I. G., Boynton, W. V., Litvak, M. L., Sanin, A. B., & Starr, R. D. (2011). Response to comment on “hydrogen mapping of the lunar south pole using the LRO neutron detector experiment lend”. *Science*, 334(6059), 1058. <https://doi.org/10.1126/science.1203483>
- Needham, D. H., & Kring, D. A. (2017). Lunar volcanism produced a transient atmosphere around the ancient Moon. *Earth and Planetary Science Letters*, 478, 175–178. <https://doi.org/10.1016/j.epsl.2017.09.002>
- Noda, H., Araki, H., Goossens, S., Ishihara, Y., Matsumoto, K., Tazawa, S., et al. (2008). Illumination conditions at the lunar polar regions by KAGUYA(SELENE) laser altimeter. *Geophysical Research Letters*, 35, 24203. <https://doi.org/10.1029/2008GL035692>
- Nozette, S., Lichtenberg, C. L., Spudis, P., Bonner, R., Ort, W., Malaret, E., et al. (1996). The Clementine bistatic radar experiment. *Science*, 274, 1495–1498. <https://doi.org/10.1126/science.274.5292.1495>

- Ong, L., Asphaug, E. I., Korycansky, D., & Coker, R. F. (2010). Volatile retention from cometary impacts on the Moon. *Icarus*, 207(2), 578–589. <https://doi.org/10.1016/j.icarus.2009.12.012>
- Paige, D. A., et al. (2018). *Lro dlre level 5 prp v2.0*. Retrieved from https://pds-geosciences.wustl.edu/lro/lro-l-dlre-4-rdr-v1/lroldr/_/1001/data/prp/
- Paige, D. A., Siegler, M. A., Harmon, J. K., Neumann, G. A., Mazarico, E. M., Smith, D. E., et al. (2013). Thermal stability of volatiles in the north polar region of Mercury. *Science*, 339(6117), 300–303. <https://doi.org/10.1126/science.1231106>
- Paige, D. A., Siegler, M. A., Zhang, J. A., Hayne, P. O., Foote, E. J., Bennett, K. A., et al. (2010). Diviner lunar radiometer observations of cold traps in the Moon's south polar region. *Science*, 330(6003), 479–482. <https://doi.org/10.1126/science.1187726>
- Pieters, C. M., Goswami, J. N., Clark, R. N., Annadurai, M., Boardman, J., Buratti, B., et al. (2009). Character and spatial distribution of OH/O on the surface of the Moon seen by on Chandrayaan-1. *Science*, 326(5952), 568–572. <https://doi.org/10.1126/science.1178658>
- Rubanenko, L., Venkatraman, J., & Paige, D. (2019). Thick ice deposits in shallow simple craters on the moon and mercury. *Nature Geoscience*, 12, 597–601. <https://doi.org/10.1038/s41561-019-0405-8>
- Sanin, A. B., Mitrofanov, I. G., Litvak, M. L., Bakhtin, B. N., Bodnarik, J. G., Boynton, W. V., et al. (2017). Hydrogen distribution in the lunar polar regions. *Icarus*, 283, 20–30. <https://doi.org/10.1016/j.icarus.2016.06.002>
- Sanin, A. B., Mitrofanov, I. G., Litvak, M. L., Malakhov, A., Boynton, W. V., Chin, G., et al. (2012). Testing lunar permanently shadowed regions for water ice: LEND results from LRO. *Journal of Geophysical Research*, 117, E00H26. <https://doi.org/10.1029/2011JE003971>
- Schorghofer, N., & Aharonson, O. (2014). The lunar thermal ice pump. *The Astrophysical Journal*, 788(2), 169. <https://doi.org/10.1088/0004-637x/788/2/169>
- Siegler, M. A., Bills, B. G., & Paige, D. A. (2011). Effects of orbital evolution on lunar ice stability. *Journal of Geophysical Research*, 116(E3), E03010. <https://doi.org/10.1029/2010JE003652>
- Siegler, M. A., Paige, D., Williams, J.-P., & Bills, B. (2015). Evolution of lunar polar ice stability. *Icarus*, 255, 78–87. <https://doi.org/10.1016/j.icarus.2014.09.037>
- Spudis, P. D., Bussey, D. B. J., Baloga, S. M., Cahill, J. T. S., Glaze, L. S., Patterson, G. W., et al. (2013). Evidence for water ice on the moon: Results for anomalous polar craters from the LRO Mini-RF imaging radar. *Journal of Geophysical Research*, 118(10), 2016–2029. <https://doi.org/10.1002/jgre.20156>
- Teodoro, L. F. A., Eke, V. R., Elphic, R. C., Feldman, W. C., & Lawrence, D. J. (2014). How well do we know the polar hydrogen distribution on the moon? *Journal of Geophysical Research: Planets*, 119(3), 574–593. <https://doi.org/10.1002/2013je004421>
- Thomson, B. J., Bussey, D. B. J., Cahill, J. T. S., Neish, C., Patterson, G. W., & Spudis, P. D. (2011). The interior of Shackleton crater as revealed by mini-RF orbital radar. In *Lunar and Planetary Science Conference* (Vol. 42, p. 1626).
- Thomson, B. J., Bussey, D. B. J., Neish, C. D., Cahill, J. T. S., Heggy, E., Kirk, R. L., et al. (2012). An upper limit for ice in Shackleton crater as revealed by LRO Mini-RF orbital radar. *Geophysical Research Letters*, 39(14), L14201. <https://doi.org/10.1029/2012GL052119>
- Trenberth, K. E., & Stepaniak, D. P. (2003). Seamless poleward atmospheric energy transports and implications for the Hadley circulation. *Journal of Climate*, 16(22), 3706–3722. [https://doi.org/10.1175/1520-0442\(2003\)016<3706:spaeta>2.0.co;2](https://doi.org/10.1175/1520-0442(2003)016<3706:spaeta>2.0.co;2)
- Vasavada, A. R., Bandfield, J. L., Greenhagen, B. T., Hayne, P. O., Siegler, M. A., Williams, J.-P., & Paige, D. A. (2012). Lunar equatorial surface temperatures and regolith properties from the Diviner Lunar Radiometer Experiment. *Journal of Geophysical Research*, 117, E00H18. <https://doi.org/10.1029/2011JE003987>
- Vasavada, A. R., Paige, D. A., & Wood, S. E. (1999). Near-surface temperatures on Mercury and the Moon and the stability of polar ice deposits. *Icarus*, 141(2), 179–193. <https://doi.org/10.1006/icar.1999.6175>
- Watson, K., Murray, B., & Brown, H. (1961). On the possible presence of ice on the Moon. *Journal of Geophysical Research*, 66, 1598–1600. <https://doi.org/10.1029/JZ066i005p01598>
- Williams, J.-P., Greenhagen, B. T., Paige, D. A., Schorghofer, N., Sefton-Nash, E., Hayne, P. O., et al. (2019). Seasonal polar temperatures on the moon. *Journal of Geophysical Research: Planets*, 124(10), 2505–2521. <https://doi.org/10.1029/2019je006028>
- Zhang, J. A., & Paige, D. A. (2009). Cold-trapped organic compounds at the poles of the Moon and Mercury: Implications for origins. *Geophysical Research Letters*, 36(16), L16203. <https://doi.org/10.1029/2009GL038614>
- Zhang, J. A., & Paige, D. A. (2010). Cold-trapped organic compounds at the poles of the Moon and Mercury: Implications for origins. *Geophysical Research Letters*, 37(3), L03203. <https://doi.org/10.1029/2009GL041806>
- Zuber, M. T., Head, J. W., Smith, D. E., Neumann, G. A., Mazarico, E., Torrence, M. H., et al. (2012). Constraints on the volatile distribution within Shackleton crater at the lunar south pole. *Nature*, 486(7403), 378–381. <https://doi.org/10.1038/nature11216>